

## LAGER Ly $\alpha$ Luminosity Function at $z \sim 7$ , Implications for Reionization

ISAK G. B. WOLD,<sup>1</sup> SANGEETA MALHOTRA,<sup>1</sup> JAMES RHOADS,<sup>1</sup> JUNXIAN WANG,<sup>2,3</sup> WEIDA HU,<sup>2,3</sup> LUCIA A. PEREZ,<sup>4</sup> ZHEN-YA ZHENG,<sup>5</sup> ALI AHMAD KHOSTOVAN,<sup>1</sup> ALISTAIR R. WALKER,<sup>6</sup> L. FELIPE BARRIENTOS,<sup>7</sup> JORGE GONZÁLEZ-LÓPEZ,<sup>8,7</sup> SANTOSH HARISH,<sup>4</sup> LEOPOLDO INFANTE,<sup>9</sup> CHUNYAN JIANG,<sup>5</sup> JOHN PHARO,<sup>4</sup> CRISTÓBAL MOYA-SIERRALTA,<sup>7</sup> FRANZ E. BAUER,<sup>7,10,11</sup> GASPAR GALAZ,<sup>7</sup> FRANCISCO VALDES,<sup>12</sup> AND HUAN YANG<sup>9</sup>

<sup>1</sup>*Astrophysics Science Division, NASA Goddard Space Flight Center, 8800 Greenbelt Road, Greenbelt, Maryland, 20771, USA*

<sup>2</sup>*CAS Key Laboratory for Research in Galaxies and Cosmology, Department of Astronomy, University of Science and Technology of China, Hefei, Anhui 230026, People's Republic of China*

<sup>3</sup>*School of Astronomy and Space Science, University of Science and Technology of China, Hefei 230026, People's Republic of China*

<sup>4</sup>*School of Earth and Space Exploration, Arizona State University, Tempe, AZ 85287, USA*

<sup>5</sup>*CAS Key Laboratory for Research in Galaxies and Cosmology, Shanghai Astronomical Observatory, Shanghai 200030, People's Republic of China*

<sup>6</sup>*Cerro Tololo Inter-American Observatory, NSF's NOIRLab, Casilla 603, La Serena, Chile*

<sup>7</sup>*Instituto de Astrofísica and Centro de Astroingeniería, Facultad de Física, Pontificia Universidad Católica de Chile, Casilla 306, Santiago 22, Chile*

<sup>8</sup>*Núcleo de Astronomía de la Facultad de Ingeniería y Ciencias, Universidad Diego Portales, Av. Ejército Libertador 441, Santiago, Chile*

<sup>9</sup>*Las Campanas Observatory, Carnegie Institution of Washington, Casilla 601, La Serena, Chile*

<sup>10</sup>*Millennium Institute of Astrophysics, Nuncio Monseñor Sótero Sanz 100, Of 104, Providencia, Santiago, Chile*

<sup>11</sup>*Space Science Institute, 4750 Walnut Street, Suite 205, Boulder, Colorado 80301*

<sup>12</sup>*National Optical Astronomy Observatory, 950 N. Cherry Avenue, Tucson, AZ 85719, USA*

### ABSTRACT

We present a new measurement of the Ly $\alpha$  luminosity function at redshift  $z = 6.9$ , finding moderate evolution from  $z = 5.7$  that is consistent with a fully or largely ionized  $z \sim 7$  intergalactic medium. Our result is based on four fields of the LAGER (Lyman Alpha Galaxies in the Epoch of Reionization) project. Our survey volume of  $6.1 \times 10^6$  Mpc<sup>3</sup> is double that of the next largest  $z \sim 7$  survey. We combine two new LAGER fields (WIDE12 and GAMA15A) with two previously reported LAGER fields (COSMOS and CDFS). In the new fields, we: identify  $N = 95$  new  $z = 6.9$  Ly $\alpha$  emitter (LAEs) candidates; characterize our survey's completeness and reliability; and compute Ly $\alpha$  luminosity functions. The best-fit Schechter luminosity function parameters for all four LAGER fields are in good general agreement. Two fields (COSMOS and WIDE12) show evidence for a bright-end excess above the Schechter function fit. We find that the Ly $\alpha$  luminosity density declines at the same rate as the UV continuum LF from  $z = 5.7$  to  $z = 6.9$ . This is consistent with an intergalactic medium that was fully ionized as early as redshift  $z \sim 7$ , or with a volume-averaged neutral hydrogen fraction of  $x_{HI} < 0.33$  at  $1\sigma$ .

### 1. INTRODUCTION

Ly $\alpha$  emission is intrinsically one of the most luminous emission lines in the ionized nebula produced by star-forming galaxies. This bright feature has enabled observational surveys to efficiently obtain large samples of Ly $\alpha$  emitting galaxies over a wide redshift range  $z = 0 - 8$  (e.g., Cowie & Hu 1998; Hu et al. 1998; Rhoads et al. 2000; Malhotra & Rhoads 2002; Ouchi et al. 2003; Gronwall et al. 2007; Gawiser et al. 2007;

Deharveng et al. 2008; Hu et al. 2010; Ouchi et al. 2010; Tilvi et al. 2020; Cowie et al. 2011; Blanc et al. 2011; Finkelstein et al. 2013; Konno et al. 2014; Matthee et al. 2015; Santos et al. 2016; Konno et al. 2016, 2018; Wold et al. 2017). These studies have revealed the general picture that Ly $\alpha$  emitters (LAEs) are young starbursting galaxies with low masses, low dust content, and high excitation states that become more common and more luminous at high-redshifts.

Furthermore, Ly $\alpha$  emission is one of the few probes of the ionization state of the intergalactic medium (IGM) during the reionization epoch (Malhotra & Rhoads 2004, 2006). We know that reionization should fall within the  $6 < z < 9$  redshift range from the saturation of Ly $\alpha$

absorbers in  $z \sim 6$  quasar spectra (Fan et al. 2006) and from polarization measurements of the cosmic microwave background (Planck Collaboration et al. 2018). Ly $\alpha$  luminosity functions and their evolution can be used to further constrain the timing of reionization because Ly $\alpha$  emission is resonantly scattered by any neutral hydrogen that it encounters, making it very sensitive to the ionization state of the IGM. Beyond a redshift of  $z \sim 6$ , previous studies have found that Ly $\alpha$  LFs decline (e.g., Konno et al. 2014; Inoue et al. 2018) at a rate exceeding the decline seen in UV LFs (e.g., Finkelstein et al. 2015; Bouwens et al. 2015). This decline may arise from the increasing opacity of the  $z \gtrsim 7$  IGM and the onset of the reionization epoch. However, the sample sizes of LAEs at the highest redshifts are still limited ( $N < 100$ ), inhibiting the current Ly $\alpha$  based reionization constraints from distinguishing between competing theoretical models (e.g., Robertson et al. 2015; Finkelstein et al. 2019; Kulkarni et al. 2019; Naidu et al. 2020). Furthermore, compiling narrow-band surveys from the literature to study the evolution of the Ly $\alpha$  luminosity functions can introduce systematics caused by differences in the adopted NB excess cut and by differences in the method used to compute the area masked by foreground sources (see discussion of selection completeness in: Hu et al. 2019). These effects can mimic redshift evolution if not properly accounted for.

With the Lyman-Alpha Galaxies in the Epoch of Reionization (LAGER) project, we are conducting a definitive  $\sim 24 \text{ deg}^2$  narrow-band Ly $\alpha$  survey at  $z = 6.9$  to precisely measure the timing and morphology of reionization. LAGER exploits DECam’s unique combination of a large 4-m aperture and  $3 \text{ deg}^2$  field of view together with a high detector sensitivity in the near-infrared. DECam’s wide field of view is needed to mitigate cosmic variance, which is expected to be amplified in any patchy reionization scenario (e.g., Jensen et al. 2014). We have designed and acquired a narrow-band filter with a central wavelength of 9642 Å that avoids strong sky OH emission lines and atmospheric absorption (Zheng et al. 2019). Consequently, LAGER is an extremely efficient Ly $\alpha$  survey at the epoch of reionization.

The LAGER collaboration has published our Ly $\alpha$  survey results from the COSMOS and CDFS fields (Zheng et al. 2017; Hu et al. 2019, 2021), spectroscopic followup of eight LAEs found within these fields (Hu et al. 2017; Yang et al. 2019), and our H $\alpha$ , [OIII], and [OII] survey results from the COSMOS field (Khostovan et al. 2020).

With the addition of the LAGER fields WIDE12 and GAMA15A, we present four out of the eight currently planned LAGER fields. Even at this nominal halfway

point, the 4-Field LAGER survey represents the largest  $z \sim 7$  Ly $\alpha$  survey to date. In this paper, we carefully correct for selection effects to study the evolution of the Ly $\alpha$  luminosity functions from  $z = 5.7$  to 6.9. We find that the evolution mirrors the decline seen in the UV LFs, which is consistent with a fully ionized  $z = 6.9$  neutral hydrogen fraction.

One of the best options to conduct unbiased large-volume surveys at high-redshift is the use of space-based grism instruments (e.g., Malhotra et al. 2005; Rhoads et al. 2009, 2013; Tilvi et al. 2016; Larson et al. 2018). These slitless spectroscopic surveys are able to avoid bright skylines that plague ground-based surveys – especially at high-redshift. The upcoming *Nancy Grace Roman Space Telescope* will have a wide-field ( $0.281 \text{ square degrees}$ ) near-infrared ( $1\text{--}1.93 \mu\text{m}$ ) grism capability that offers the opportunity to revolutionize  $z > 8$  Ly $\alpha$  surveys. The LAGER project provides a reference  $z \sim 7$  Ly $\alpha$  survey that can be used in combination with upcoming  $z > 8$  *Roman* surveys to study the evolution of the Ly $\alpha$  population and further constrain the ionization state of the IGM.

Throughout this work, all Ly $\alpha$  equivalent widths (EWs) are rest-frame and all magnitudes are in the AB magnitude system ( $m_{\text{AB}} = 31.4 - 2.5 \log_{10} f_\nu$  with  $f_\nu$  in units of nJy). We adopt a flat  $\Lambda$ CDM cosmology with  $\Omega_m = 0.3$ ,  $\Omega_\Lambda = 0.7$ , and  $H_0 = 70 \text{ km s}^{-1} \text{ Mpc}^{-1}$ .

## 2. OBSERVATIONS

We observed LAGER fields WIDE12 and GAMA15A with the Blanco 4-m telescope at Cerro Tololo Interamerican Observatory (CTIO) using the Dark Energy Camera (DECam) instrument and the narrow-band NB964 filter. NB964 has a central wavelength of 9642 Å and a narrow FWHM of 92 Å that was custom-made to avoid bright skylines and atmospheric absorption (Zheng et al. 2019). Given two surveys with the same limiting NB magnitude, a narrower FWHM has less bandpass dilution and is able to detect fainter emission line sources. A pure emission line source will be  $\sim 0.8$  magnitudes brighter in our survey compared to a NB survey with twice our FWHM (e.g., Ota et al. 2017), and a Ly $\alpha$  emitter with a rest-frame EW = 10 Å will be  $\sim 0.3$  magnitudes brighter in our survey. The DECam instrument is an optical imager that has 62 CCDs covering a 2.2-degree diameter field of view with a 0.264 arc-sec pixel scale. Data were obtained over 20 nights and 6 observing semesters (NOAO PID: 2017A-0366; 2017A-0920; 2018A-0371; 2018B-0327; 2018B-0907; 2019A-0912). In total, we observed WIDE12 for 100.6 ks and GAMA15A for 85.3 ks and obtained a  $5\sigma$  point source

**Table 1.** Exposure Time, Seeing, and Image Depth

Field	Filter	Exp. Time (ks)	Seeing (arcsec)	Aperture $5\sigma$ Depth (AB mag)	Total $5\sigma$ Depth (AB mag)	Depth Aperture (Diameter in arcsec)
WIDE12	NB964	100.6	1.10	25.3/24.7	24.6/24.3	1.2/1.8
12 <sup>h</sup> 04 <sup>m</sup> 25 <sup>s</sup>	HSC-y	1.2	0.67	24.8/24.4 <sup>psf</sup>	24.4/24.1 <sup>psf</sup>	1.0/1.8 <sup>psf</sup>
0°00′00″	HSC-griz	3.6	0.63	27.0/26.1	26.7/26.0	1.0/1.8
(J2000)	HSC-z	1.2	0.68	25.9/25.1	25.5/25.0	1.0/1.8
	HSC-i	1.2	0.59	26.5/25.7	26.2/25.6	1.0/1.8
	HSC-r	0.6	0.59	26.7/25.8	26.3/25.7	1.0/1.8
	HSC-g	0.6	0.72	27.0/26.2	26.5/26.0	1.0/1.8
GAMA15A	NB964	85.3	1.03	25.2/24.6	24.6/24.3	1.2/1.8
14 <sup>h</sup> 22 <sup>m</sup> 00 <sup>s</sup>	HSC-y	1.2	0.80	25.0/24.4 <sup>psf</sup>	24.4/24.1 <sup>psf</sup>	1.0/1.8 <sup>psf</sup>
0°00′00″	HSC-griz	3.6	0.61	27.0/26.0	26.6/25.9	1.0/1.8
(J2000)	HSC-z	1.2	0.71	25.8/24.9	25.3/24.8	1.0/1.8
	HSC-i	1.2	0.58	26.5/25.7	26.2/25.6	1.0/1.8
	HSC-r	0.6	0.54	26.6/25.7	26.3/25.7	1.0/1.8
	HSC-g	0.6	0.72	27.0/26.2	26.5/26.0	1.0/1.8

<sup>psf</sup>The  $y$ -band D = 1.8"  $5\sigma$  depth measurements are computed for the HSC image that is PSF-matched to the NB DECam image. All other HSC depths are computed at native resolution.

survey depth of  $\sim 25$  mag with 1 arcsec seeing for both fields. We used a  $4' \times 4'$  five-pointing ‘X’ shaped dither pattern which we repeated, offsetting the entire pattern randomly by up to  $30''$  for each new set of five exposures.

We supplement our NB964 data with overlapping Hyper Suprime-Cam Subaru Strategic Program (HSC-SSP) *grizy* DR2 broadband images (Aihara et al. 2018). HSC is an optical imager on the 8.2m Subaru Telescope that has 104 CCDs covering a 1.5-degree diameter field of view with a 0.168 arcsec pixel scale. The HSC-SSP is a three-layered multi-band survey that consists of a Wide, Deep, and Ultradeep layer. Our LAGER WIDE12 and GAMA15A fields are fully contained within the HSC-SSP Wide layer which has 5 broadband images with 0.6 arcsec seeing and a  $5\sigma$  point source depth of  $\sim 26$  mag. We obtained HSC Pipeline (Bosch et al. 2018) calibrated broadband mosaic images via their public database<sup>1</sup>. We use the HSC  $y$ -band to select  $y$ -NB excess objects, and we use the HSC *griz*-bands as veto bands to help reject low-redshift interlopers.

### 3. DECAM AND HSC MOSAIC IMAGES

#### 3.1. DECam Image Stacking

We collected all the WIDE12 and GAMA15A NB964 InstCal images associated data quality maps (DQMs) observed before August 2019 from the NOAO Science

Archive<sup>2</sup>. NOAO InstCal images are processed through the Community Pipeline (CP; Valdes et al. 2014) to remove instrumental effects and to perform an initial photometric and astrometric calibration. For our specialized analyses, we require astrometric and photometric calibrations beyond those produced by the CP, and for this reason, we recalibrate using a procedure as described in Wold et al. (2019). Here we outline this astro-photometric calibration and image stacking method with emphasis on alterations made to accommodate our NB964 data.

Consistent with the HSC-SSP (Aihara et al. 2018), we use the Pan-STARRS1 (PS1) Data Release 2 catalog (Chambers et al. 2016) as our astro-photometric reference. PS1 is a *grizy*-band 30,000 deg<sup>2</sup> survey that has millimag photometric and milliarcsec astrometric calibration. The PS1 *grizy*-band  $5\sigma$  point source depths are 23.3, 23.2, 23.1, 22.3, and 21.4, respectively. For each DECam exposure, we identify SNR  $> 10$  stars with no neighboring objects within  $r = 8''$  and determine the median x- and y-offset needed to align our images to PS1. For each exposure, we measure the seeing, the background rms, and the relative flux scaling factors required to adjust all images to a designated NB964 reference image.

With these measurements in hand, we produce image mosaics using SWarp (Bertin et al. 2002) employing

<sup>1</sup> <https://hsc-release.mtk.nao.ac.jp>

<sup>2</sup> <http://archive1.dm.nao.edu/>

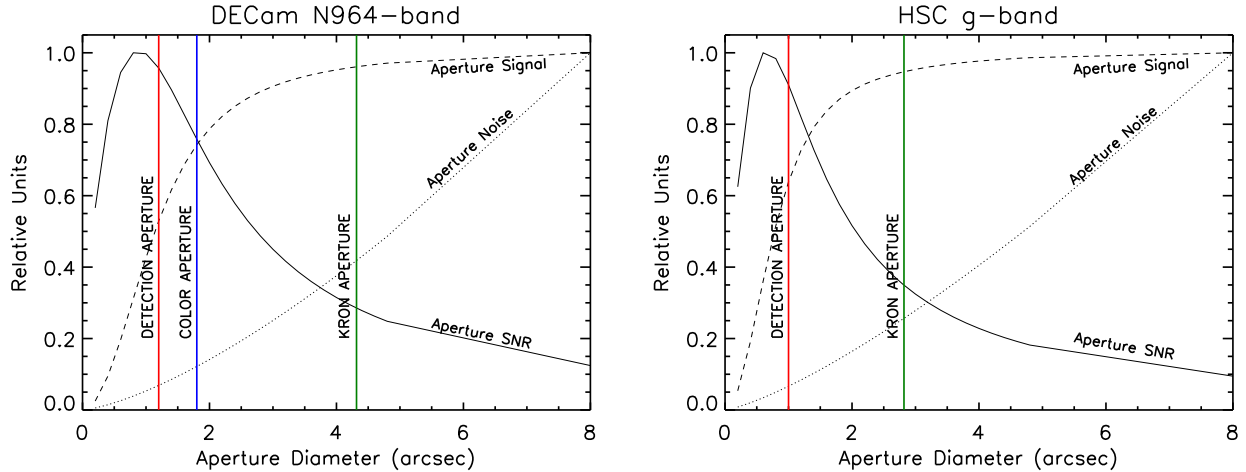


**Figure 1.** Demonstration of our method for determining the optimal PSF aperture for field WIDE12. The dotted, dashed, and solid curves show how the noise, signal, and SNR vary with aperture size. For display purposes, all curves are normalized to a maximum value of unity. The red vertical line shows our adopted optimal extraction aperture, labeled as the ‘detection aperture’. These apertures are slightly larger than the value at the peak of the SNR curve to help mitigate systematic errors such as errors introduced by non-perfect image co-alignment. The blue vertical line shows our adopted aperture to measure  $y$ -NB964 colors, labeled as the ‘color aperture’. As shown in Figure 2, we find that  $1.8''$  apertures outperform Kron apertures when measuring  $y$ -NB964 colors. For comparison, the green vertical line shows the median SE Kron aperture for point sources. The behavior for other filters and for our other field, GAMA15A, are similar to the results shown here. For both fields, we use a  $1.0''$  detection aperture for the HSC  $griz$  bandpasses, and we use a  $1.2''$  detection aperture for the DECam NB964 bandpass.

point-source-optimized weighting (Gawiser et al. 2006). When stacking, we assign zero weight to pixels flagged by the NOAO DQMs which identify detector defects and image artifacts such as bleed trails, saturation, and cosmic rays. Despite this practice, we find that in some cases cosmic rays and satellite trails are not fully masked in the resulting stacked image. Consequently, we employed our own artifact removal procedure which is based on the algorithm presented by Gruen et al. (2014). To implement this procedure we produce a PSF-matched median stack and flag pixels from individual PSF-matched science exposures as bad if they significantly differ from the median stack. Defining  $f_i$  as the pixel flux of exposure  $i$  and  $\mu$  as the median pixel flux of all exposures, we flagged pixels that met the following criteria:

$$|f_i - \mu| > n\sigma_i + A|\mu| \quad (1)$$

where  $\sigma_i$  is the pixel noise and  $n$  and  $A$  are empirically determined clipping parameters that set the statistical and PSF related leniency of the procedure. For our images which were already flagged for artifacts with the NOAO pipeline, we used  $n = 5$  and  $A = 0.7$  to flag the remaining artifacts. Our procedure results in revised DQMs that contain both the NOAO DQM flags (masking  $\sim 3\%$  of image pixels) and our own artifact flags (masking  $\sim 0.1\%$  of image pixels). We use these revised DQMs to flag bad pixels in non-PSF-matched exposures

when producing our final point-source-optimized image mosaics.

We photometrically calibrate our final NB mosaics using the PS1  $z$ - and  $y$ -bands which bookend our NB964 bandpass. As described in Wold et al. (2019), we assume a linear color relation between PS1 and NB964 magnitudes for point sources, such that:

$$z_{\text{PS1}} = \text{NB964} + \alpha(z_{\text{PS1}} - y_{\text{PS1}}) + \text{ZPT} \quad (2)$$

We determine the color slope ( $\alpha$ ) and the required zero-point offset (ZPT) needed to adjust our NB magnitudes to AB by solving for the best-fit line. We report the characteristics of our NB mosaics and the accompanying broad band (BB) mosaics in Table 1.

### 3.2. Source Extraction

We use SExtractor (SE; Bertin & Arnouts 1996) in dual-image mode to produce narrow-band selected catalogs. To run SE in double-image mode, the NB detection image and the BB measurement image must have the same dimensions. However, the HSC images have a smaller pixel scale and a different pixel grid than our NB DECam mosaics. Given this mismatch, we investigate two methods to produce the desired NB-selected catalogs. 1) Following Hu et al. (2019), we resample HSC’s BB images ( $grizy$ -bands) to match DECam’s pixel scale and then generate the desired NB-selected catalog from these co-registered images. 2) We create a synthetic NB detection image with the same dimensions and pixel



scale as the BB mosaics. Sources within the synthetic NB detection image have Gaussian profiles (FWHM = 2 HSC pixels or  $0.336''$ ) with coordinates determined from the NB catalog. The main requirement for these inserted Gaussian sources is that SE can reliably detect and locate them, and this procedure is merely a stratagem to have SE perform aperture photometry on all the BB images at the coordinates of all NB objects. With this second method, we produce NB-selected catalogs for the HSC *grizy*-band data without having to resample and thus degrade the HSC data.

One potential drawback of this second method is the inability to use SE Kron flux measurements. Kron apertures are adaptive ellipses designed to capture  $\sim 95\%$  of the total flux for both extended and unresolved sources (Kron 1980; Bertin & Arnouts 1996). For LAGER fields COSMOS and CDFS, we used these apertures to accurately measure  $y$ -NB colors for both extended and point-like sources. In dual-image mode, Kron apertures are based on the detection image morphology and by making a synthetic detection image we lose the NB morphology constraints. In Section 4, we compare Kron colors measured from the resampled  $y$ -band image to aperture colors measured from a  $y$ -band image PSF-matched to our NB mosaic.

To help identify foreground emitters, we also produced a point-source-optimized stack for all bandpasses blueward of our NB filter, thus producing a combined *griz* master veto band.

As discussed in Section 4, we ultimately use the following NB-selected catalogs in the final LAE selection: 1) the non-resampled  $g, r, i, z, griz$  veto band catalogs for elimination of foreground objects and 2) the PSF-matched  $y$ -band catalog for NB-excess measurements.

For all catalogs, we exclude objects that fall within our bright star mask. The regions around bright stars have much higher background levels effectively masking out regions of the sky and causing spurious detections due to diffraction spikes and saturation effects. We mitigate these issues by masking out all 2MASS point sources (Cutri et al. 2003) with  $J$ -band magnitudes brighter than 13. Following the procedure outlined in Keenan et al. (2010) and Wold et al. (2019), we determined a magnitude dependent circular star mask with the arc-second Radius defined by:

$$\text{Radius} = 326.3 - 41.2J + 1.4J^2 \quad (3)$$

where the three coefficients are empirically determined parameters set to remove spurious detections around bright stars. With the star mask applied, we compute our survey area as  $3.24 \text{ deg}^2$  in WIDE12 and  $2.91 \text{ deg}^2$  in GAMA15A.

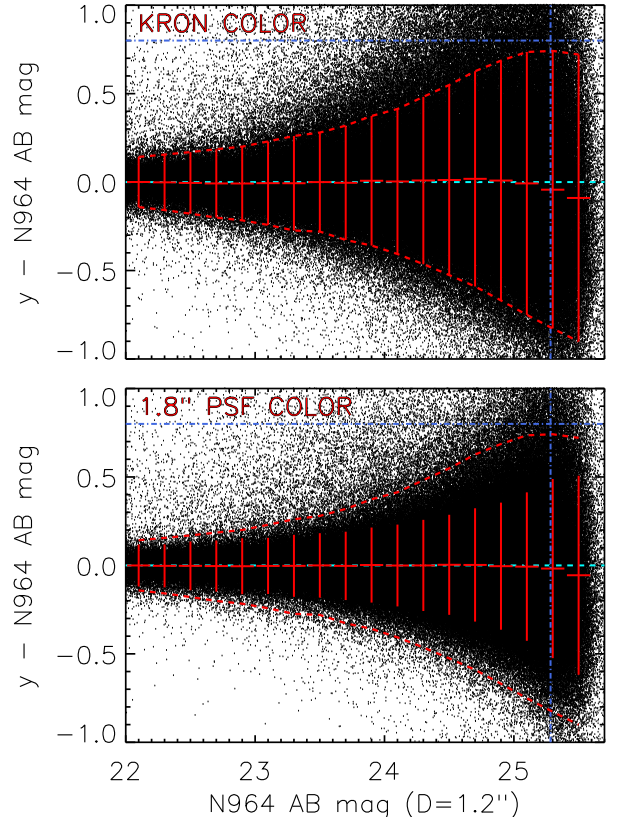


**Figure 2.** (Top)  $y$ -NB color determined with Kron apertures as a function of NB  $D=1.2''$  aperture magnitude for sources in WIDE12. The red data-points show the binned median color and their error bars show the standard deviation of the binned color measurements. The horizontal blue dashed line shows the  $y$ -NB  $> 0.8 \text{ mag}$  color selection used to isolate LAEs. The vertical blue dashed line shows the  $5\sigma$  NB detection limit. (Bottom) The same as the top, but colors are measured with PSF-matched  $D=1.8''$  apertures. The systematic errors measured by the locations of the binned median colors are comparable to the Kron results. However, the random error measured by the binned color standard deviations are significantly reduced. For this reason, we adopt PSF-matched  $1.8''$  colors for our LAE selection in both WIDE12 and GAMA15A fields (see Figure 3). In both the top and bottom figures, we show the envelope of the Kron color data points (dashed red curves) for easy comparison between the two results.

#### 4. LAE CANDIDATES

We wish to isolate a relatively small sample of  $z = 6.9$  LAEs from our NB-selected catalogs which contain  $N \sim 530,000$  objects per field. The first step toward this goal is to identify the optimal aperture size to measure the flux of our NB-selected objects. Of particular interest are relatively compact sources, such as the targeted  $z = 6.9$  LAEs and one of our most challenging contaminants, high-EW foreground emitters. To this end, we

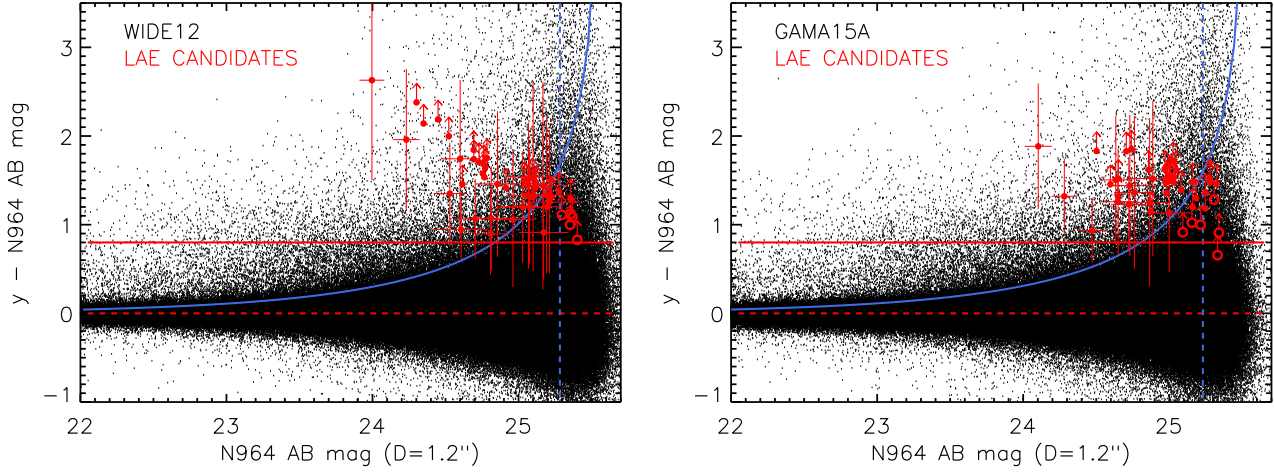


**Figure 3.** To illustrate our LAE candidate selection, we show the NB color excess as a function of NB  $D=1.2''$  aperture magnitude for both WIDE12 and GAMA15A fields. The vertical dashed line indicates the median  $5\sigma$  depth of the NB image. The horizontal red line indicates the 0.8 mag  $y$ -NB color cut. The blue solid curve indicates the median  $2\sum$  NB excess flux significance. LAE candidates (red data points) satisfy all selection cuts as described in Section 4.  $y$ -NB color lower limits (red arrows) are shown for candidates that are not detected above  $1\sigma$  in the  $y$ -band. Individual LAE candidates can fall below the median selection cuts in the panels above, primarily in cases where the local image depth is better than the median image depth. LAE candidates that have completeness corrections less than 5% are excluded from our luminosity function computation and are displayed above with open red circles (for details see Section 6)

investigate which aperture size maximizes the SNR for point sources. We estimate the signal as a function of aperture size by measuring the median aperture flux relative to the total flux in  $0.2''$  intervals for our isolated star sample. In other words, we compute the median curve of growth for point sources, where  $8''$  diameter apertures are used to measure the total flux. For noise measurements, we randomly place  $N = 10,000$  sky apertures within our science images and compute the median absolute deviation of these measured aperture fluxes (for a similar procedure see Gawiser et al. 2006; Wold et al. 2019).

In Figure 1, we show how these quantities and their ratio, the SNR for point sources, vary with aperture size. For both fields, we adopt  $1.2''$  diameter apertures to measure DECam fluxes and  $1.0''$  diameter apertures to measure HSC fluxes. We refer to these apertures as our detection apertures. We chose apertures that are slightly larger than the value at the peak of the SNR curve to help mitigate systematic errors such as errors introduced by non-perfect image co-alignment.

The second step toward isolating a sample of  $z = 6.9$  LAEs is to accurately determine  $y$ -NB colors for both extended and unresolved sources. Hu et al. (2019) showed that a color cut of  $y$ -NB  $> 0.8$  mag cleanly isolates strong  $\lambda_{\text{OBS}} = 9642 \text{ \AA}$  emitters ( $\text{EW} \gtrsim 10 \text{ \AA}$  for LAEs) from the more general continuum population. Ideally, our adopted method for measuring color should maximize the  $y$ -NB SNR while minimizing systematic

errors that can be introduced by image co-registration, differential seeing, and differential image depth. To maximize the color SNR we would like to use apertures with sizes similar to our detection apertures, and Gawiser et al. (2006) develop a method to use optimal detection apertures to measure colors for both resolved and unresolved sources. This method derives aperture corrections by estimating each object’s intrinsic size from the detection image. However, the relatively poor seeing of our NB detection image compared to the HSC  $y$ -band seeing – which in some cases results in unresolved NB objects with resolved BB counterparts – means that we are unable to accurately measure intrinsic sizes and aperture corrections using this method.

In Figure 2, we show the two methods that we considered to determine  $y$ -NB colors: Kron aperture colors and PSF-matched aperture colors. The main disadvantage of using Kron apertures is their large size. For point sources within our NB mosaics, the use of Kron apertures degrades the aperture SNR by a factor of three relative to our detection aperture (see Figure 1).

Our PSF-matched colors use smaller, more optimal apertures, at the expense of having to smooth the measurement image to the detection image’s PSF. In Figure 2, we show that our PSF-matched aperture size of  $1.8''$  has systematic errors comparable to Kron apertures but significantly reduces the  $y$ -NB color scatter. Given the reduced color scatter shown in Figure 2, we chose to use

1.8'' PSF-matched colors over Kron aperture colors in our LAE selection.

For WIDE12 and GAMA15A, we select LAEs using 1.8'' PSF-matched apertures when relative measurements are needed and otherwise use detection apertures via:

$$\begin{aligned} \text{SNR}_{1.2''}(\text{NB964}) > 5 \ \& \ \text{SNR}_{1.0''}(g, r, i, z, \text{griz}) < 3 \ \& \\ \Sigma_{1.8''} > 2 \ \& \\ [(y_{1.8''} - \text{NB964}_{1.8''} > 0.8 \ \& \ \text{SNR}_{1.8''}(y) > 3) \ \text{or} \ \text{SNR}_{1.8''}(y) < 3] \end{aligned} \quad (4)$$

where

$$\Sigma_{1.8''} = \frac{f_{1.8''}(\text{NB964}) - f_{1.8''}(y)}{\sqrt{\sigma_{1.8''}^2(\text{NB964}) + \sigma_{1.8''}^2(y)}} \quad (5)$$

Our selection is similar to the previous LAGER studies (Hu et al. 2019; Zheng et al. 2017). The only differences are the use of PSF-matched aperture colors rather than Kron aperture colors, the explicit use of a combined *griz* veto band, and the use of the  $\Sigma$  parameter (Bunker et al. 1995; Sobral et al. 2013; Matthee et al. 2015; Coughlin et al. 2018) which measures the significance of the NB flux excess. In the previous LAGER fields (COSMOS and CDFS) the available broadband images used to determine the NB excess were 1-2 magnitudes deeper than the NB images (Hu et al. 2019), and a  $5\sigma$  NB detection with the (narrow – broad) color of a line emitter was guaranteed a significant NB flux excess. For our WIDE12 and GAMA15A fields, the broadband images have about the same depth as the NB images (see Table 1), and the  $\Sigma$  parameter is needed to guarantee a clean selection of emitters at faint NB magnitudes. Negative  $y$ -band fluxes can boost our  $\Sigma$  parameter; however, we have verified that replacing negative  $y$ -band fluxes with zero does not change our final list of LAE candidates.

The overall filter set for the new fields is the same as for COSMOS. Thus, based on analysis in fig. 2 of Hu et al. (2019), the  $\text{Ly}\alpha$  equivalent width threshold for inclusion in our sample is  $\text{EW}_{\text{rest}} \gtrsim 10\text{\AA}$  (or  $\text{EW}_{\text{obs}} \gtrsim 80\text{\AA}$ ), with some dependence of the threshold on line wavelength (i.e., on precisely where the emission line falls within the filter transmission curve). This is modified at the faintest NB964 magnitudes in the sample, where the  $\Sigma > 2$  criterion in equation 4 is more stringent than the  $y - \text{NB964} > 0.8$  criterion, and the effective equivalent width threshold rises accordingly by a factor  $\lesssim 2$ . This can be seen in Figure 3, where we illustrate the cuts used to isolate our LAE candidates.

The WIDE12 and GAMA15A veto bands are  $\sim 1$  magnitude shallower than in the COSMOS and CDFS fields. To mitigate contamination from faint foreground

emitters, we combine all the available veto bandpasses to construct a master *griz* veto image and require our candidates to be undetected at the  $3\sigma$  limit (see Section 5 for discussion of the purity of our sample).

We find 149 and 131 LAE candidates in our WIDE12 and GAMA15A fields, respectively. Visual inspection was performed independently by three of the authors. All LAE candidates were visually verified by inspecting all available bandpasses ( $g, r, i, z, \text{griz}, y, \text{NB}$ ) for potential problems. The three visual classifications were found to largely agree. Artifacts, such as diffraction spikes and cosmic rays, contaminated our candidate list at the 25% level, while sources with weak counterparts in one of the veto bands but below our formal  $3\sigma$  cut contaminated our candidate list at the 41% level. We find a final clean sample of  $N = 50$  and  $N = 45$  LAE candidates in the WIDE12 and GAMA15A fields, respectively. This more than doubles the LAGER LAE sample size from  $N = 79$  (Hu et al. 2019) to  $N_{\text{4-Field}} = 174$ .

We compute  $\text{Ly}\alpha$  line fluxes from the aperture corrected NB and BB  $D = 1.8''$  fluxes. For LAEs with undetected BB fluxes, we use  $1\sigma$   $y$ -band measurements to estimate BB flux. We assume the LAE candidates have a  $\delta$ -function  $\text{Ly}\alpha$  line profile at the center of the NB filter and a UV continuum slope of  $-2$  that is attenuated by the IGM via the Inoue et al. (2014) model. Given this assumed spectral shape, the NB/BB filter responses, and the NB/BB fluxes we solve for the normalization of the UV continuum and the  $\text{Ly}\alpha$  flux (for a similar procedure see Hu et al. 2019).

In Figure 4, we show the spatial distribution of our final LAE candidate sample for both fields. Within our two fields, we find about the same number  $N = 6$  of bright  $\log(L_{\text{Ly}\alpha}) > 43.3 \text{ erg s}^{-1}$  LAE candidates (red filled circles) as found by Hu et al. in LAGER fields COSMOS and CDFS where  $N = 7$ . Furthermore, we notice large field-to-field variation with both the WIDE12 and COSMOS fields displaying a higher concentration of bright LAEs relative to the GAMA15A and CDFS fields. Unlike what was found in the LAGER COSMOS field, we do not find bright LAEs preferentially in LAE over-densities. This could reflect field-to-field variation, or our fields might not be deep enough to detect the faint LAEs within the over-densities. Our minimum  $\text{Ly}\alpha$  luminosity is  $\sim 10^{42.8}$ , while the minimum luminosity for the CDFS and COSMOS fields is  $\sim 10^{42.6} \text{ erg s}^{-1}$ .

## 5. RELIABILITY OF THE LAE SAMPLE

We estimate the foreground contamination in LAE samples from the new WIDE12 and GAMA15 fields using deeper images from the LAGER COSMOS field.



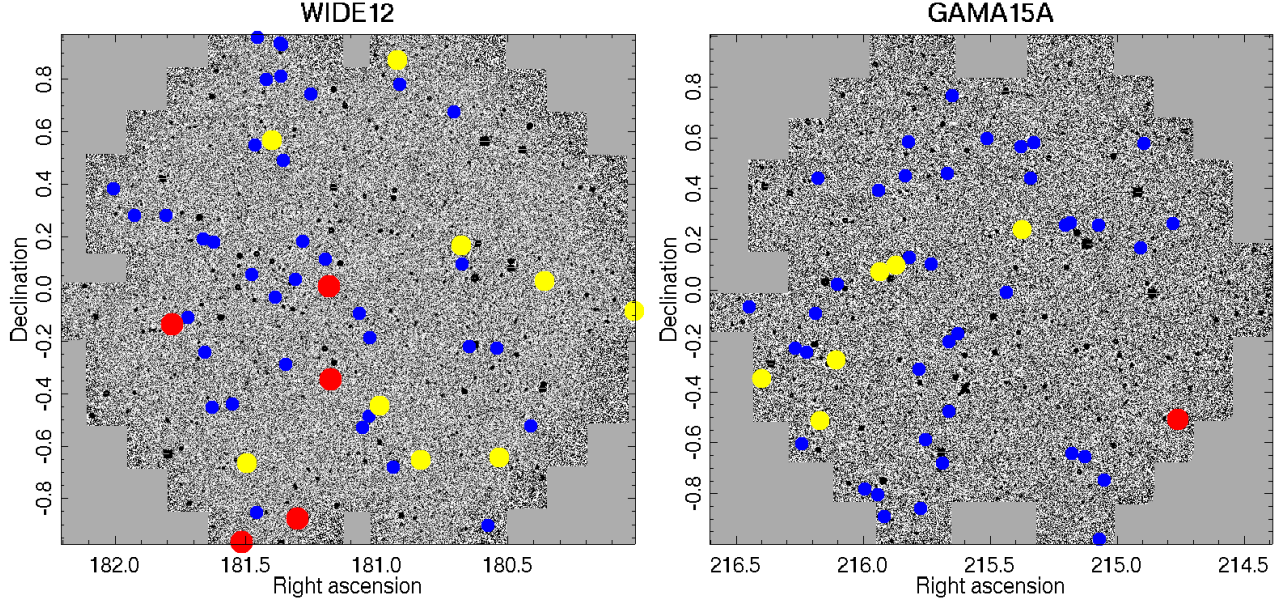


**Figure 4.** Spatial distribution of our  $z = 6.9$  Ly $\alpha$  emitters. Red, yellow, and blue filled circles indicate LAEs with  $L_{\text{Ly}\alpha} > 10^{43.3}$ ,  $10^{43.1-43.3}$ , and  $< 10^{43.1} \text{ erg s}^{-1}$ . Unlike the LAGER COSMOS field, we do not find bright LAEs preferentially in LAE over-densities. This could reflect field-to-field variation, or our fields might not be deep enough to detect the faint LAEs within the over-densities. Our minimum Ly $\alpha$  luminosity is  $\sim 10^{42.8}$ , while the minimum luminosity for the CDFS and COSMOS fields is  $\sim 10^{42.6} \text{ erg s}^{-1}$ . Both fields display  $D \sim 40'$  voids that corresponds to 12.5 pMpc at  $z = 6.9$ .

We ask two related questions. (a) First, how many emission line galaxies in COSMOS have measured veto filter fluxes lying between the  $3\sigma$  limit for COSMOS and the brighter  $3\sigma$  limit for WIDE12 and GAMA15? Such galaxies would be LAE candidates in our shallower fields, but would be correctly ruled out as foreground emitters given deeper data. (b) Second, if we randomly perturb the measured fluxes in the COSMOS emission line catalog, adding noise to simulate the depth of the shallower fields, how many other galaxies will scatter into the LAE selection region?

COSMOS has archival HSC veto bandpass data typically deeper by 1 – 2 magnitudes, along with published photo- $z$  measurements based on 30-band photometry (Laigle et al. 2016). By using the existing COSMOS catalog of foreground emitters (Khostovan et al. 2020) and artificially degrading the depth to match the WIDE12 and GAMA15 depths, we can estimate the number of foreground emitters contained within the WIDE12 and GAMA15 LAE candidate lists.

We begin with Khostovan et al.’s NB964-selected COSMOS catalog of  $N = 10,877$  EW $_{\text{OBS}} > 52.2 \text{ \AA}$  H $\alpha$ , [OIII], and [OII] emitters which is photo- $z$  and color selected based on Laigle et al.’s COSMOS2015 catalog ( $B, r, i, z, y$  with  $5\sigma$  depths of 26.4, 25.9, 25.6, 25.3, 24.2). Khostovan et al.’s catalog selects emitters down to a  $5\sigma$  NB depth of 25.45. This is  $\sim 0.8$  magnitudes deeper than our WIDE12 and GAMA15A fields, where the total  $5\sigma$  depth is 24.6. Furthermore, the NB magnitude dis-

tribution for the selected foreground emitters peaks at  $\sim 24.5$ , which is comparable to our WIDE12/GAMA15 NB depth limit.

We cross-match this foreground emitter catalog to the HSC Subaru Strategic Program DR2 catalog ( $g, r, i, z, y$  with  $5\sigma$  depths of 27.3, 26.9, 26.7, 26.3, 25.3). We perform this cross-match for two reasons: 1) our LAE selection employs HSC bandpasses and 2) the HSC DR2 survey is  $\sim 1$  magnitude deeper than Laigle et al.’s COSMOS2015 catalog.

We find the closest cataloged HSC DR2 match within a  $1.5''$  search radius of the emitter’s coordinate. We accept the match if a  $|r_{\text{Laigle}} - r_{\text{HSC}}| < 1 \text{ mag}$  or  $r_{\text{Laigle}} > 26 \text{ mag}$ , where the  $5\sigma$  depth of  $r_{\text{Laigle}}$  is  $\sim 26 \text{ mag}$ . Our adopted condition for accepting a cross-match is designed to default to the Laigle et al. catalog – the catalog used to identify foreground emitters – when there are significant conflicts between the two surveys. We find that 90% of the foreground emitters have an accepted match, and record their HSC magnitudes. For the remaining 10%, we record their Laigle et al. magnitudes. Visually inspecting the objects with no accepted HSC match, they appear to be dominated by HSC DR2 background subtraction issues around bright stars and deblending issues. For these objects, we regard the Laigle et al. catalog to be more reliable, and our catalog cross-matching method ensures that the Laigle et al. flux values are used.

For the purposes of this foreground contamination estimate, we use our field’s total bandpass depths (see Table 1) and HSC DR2’s CModel total magnitudes which are designed to measure total fluxes for both extended and point sources (Bosch et al. 2018). For the small percentage of sources with only COSMOS2015 magnitudes, we use their cataloged Kron magnitudes to measure total fluxes.

Using this final catalog of foreground emission line galaxy fluxes, we find five galaxies that are securely identified as foreground emitters in COSMOS, but whose measured veto band fluxes would fall below the  $3\sigma$  threshold given the shallower broad-band imaging depths of either the WIDE12 or the GAMA15 field.

To further explore the impact of photometric errors on our sample contamination, we perform a simple simulation to see how many galaxies scatter into our LAE selection region in color space. For each object in the input (COSMOS) catalog, we perturb the photometry, adding an amount of random noise to reproduce the photometric uncertainties of WIDE12 and GAMA15. We independently perturb the test catalog 10,000 times, each time applying our LAE selection criteria (Equation 4). Averaging over all the runs, we find  $5.1 \pm 1.5$  contaminants for WIDE12 and  $5.6 \pm 1.6$  contaminants for GAMA15A. These foreground emitters typically have NB-magnitudes ranging from 23.5 – 24.1 and high equivalent widths ( $EW_{\text{OBS}} > 180\text{\AA}$ ).

We find  $N = 45\text{--}50$  LAEs per new LAGER field and this indicates a  $f_{\text{cont}} \sim 11\%$  contamination rate. However, the COSMOS LAE selection is performed over a slightly smaller area when compared to our current fields. Correcting for our slightly larger area,

our Monte Carlo procedure yields a  $\pm 1\sigma$  range of  $f_{\text{cont}} = 10 - 19\%$  contamination in our WIDE12 and GAMA15A LAE sample.

Our foreground contamination estimate neglects any field-to-field variation by assuming the COSMOS field is representative of our other LAGER fields. We emphasize that spectroscopic follow-up has been very successful with an 80% recovery rate found in a Keck/LRIS follow-up of 21 LAE candidates (Harish et al. 2021). Based on our best catalog-based estimate and based on our on-going follow-up, we expect some moderate level of contamination in our LAE sample which is consistent with archival Ly $\alpha$  surveys (e.g., Konno et al. 2018, estimate  $f_{\text{cont}} = 17 - 33\%$ ).

## 6. COMPLETENESS OF THE LAE SAMPLE

We insert artificial LAEs into our NB and BB science images and then extract, measure, and select Ly $\alpha$  candidates using our standard procedure explained in Sec-

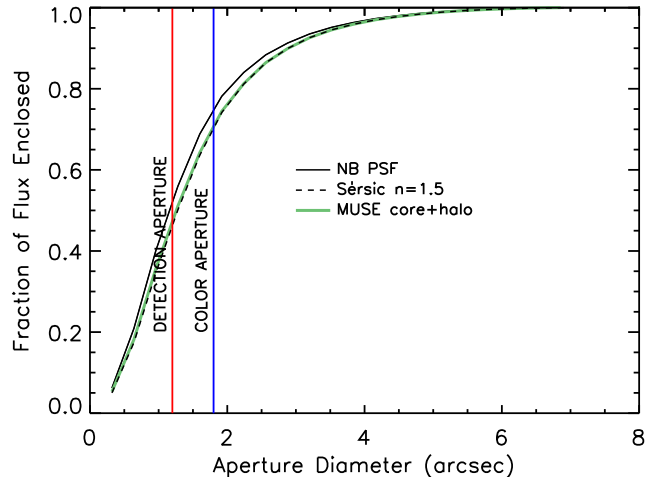


**Figure 5.** Comparison between our simulated MUSE-inspired profile (green curve) and the Sérsic  $n=1.5$  profile used by recent  $z \sim 7$  LAE surveys (black dashed curve, Konno et al. 2018; Hu et al. 2019). Both are convolved with our NB PSF (black solid curve). Given the similarity between these spatial profiles, we simulate LAEs with a Sérsic  $n=1.5$  profile to be consistent with past studies.

tions 4. We use the number of recovered objects over the number of input objects per NB magnitude bin to estimate our sample’s completeness.

For completeness measurements, the MUSE LAE surveys at  $z = 3 - 6$  (Wisotzki et al. 2016; Leclercq et al. 2017; Herenz et al. 2019) have emphasized the need to account for the LAE’s extended spatial profiles. These studies found significant LAE diffuse halos which, if not properly accounted for, can result in a factor of  $\sim 2$  under-estimates of the faint-end of the LAE LF. Furthermore, Wisotzki et al. find that higher-redshift LAEs tend to have smaller halo scale lengths and higher-EW LAEs tend to have lower halo flux fractions. Given these trends and our high-redshift, high-EW LAE sample, we made simulated LAEs with 1) a halo exponential scale length of 1 kpc, 2) a core exponential scale length of 0.1 kpc, and 3) a halo flux fraction of 0.4. We expect the LAE population to display a distribution of spatial profiles. However, observational constraints on this distribution and potential dependences on physical quantities are lacking especially at the highest redshifts. Given these uncertainties, we used a single spatial profile in our completeness simulations.

In Figure 5, we show that there is little difference between our simulated MUSE-inspired profile and a Sérsic  $n=1.5$  profile with a half-light radius of 0.9 kpc used by previous high-redshift LAE surveys (Konno et al. 2018; Hu et al. 2019) once convolved with our NB PSF. Given this result and for consistency with past studies, we simulate LAEs with a Sérsic  $n=1.5$  profile for both their NB



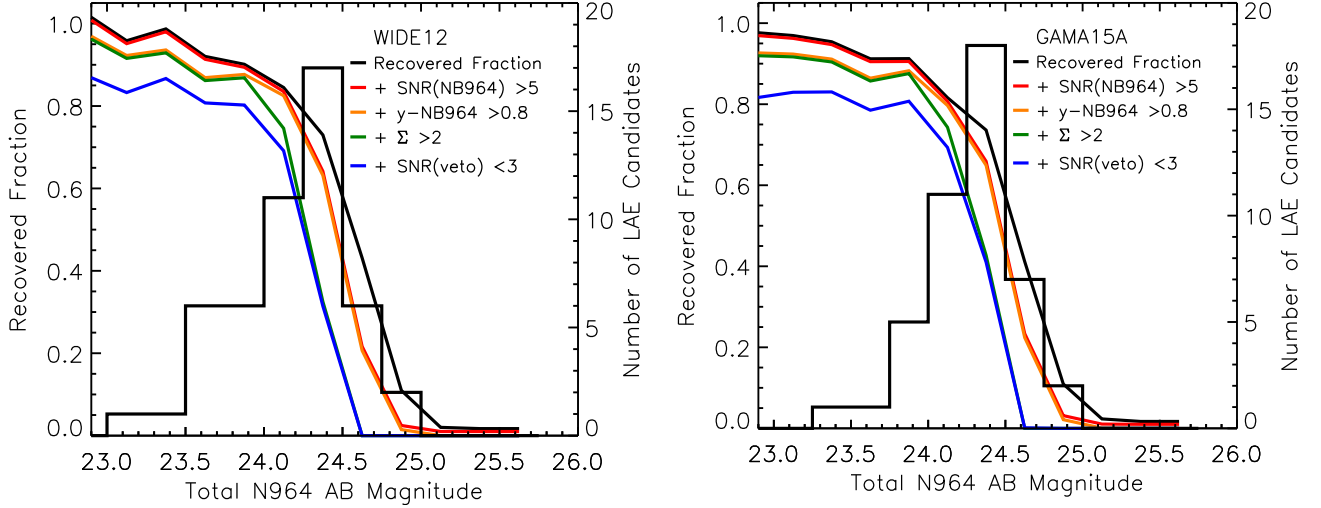


**Figure 6.** WIDE12 and GAMA15A LAE completeness curves as a function of total NB magnitude. We show the effect of sequentially applying our LAE selection cuts with the red, orange, green, and blue completeness curves. The black histogram indicates the NB magnitude distribution of our LAE candidates. By convention, simulated sources are not prevented from falling within the isophotes of real sources. Thus, the measured flux from the recovered source can be boosted. Additionally, inputted sources have their NB and BB flux altered by the background noise which can cause sources to scatter into adjacent magnitude bins. In practice our total completeness (blue curve) never exceeds  $\sim 85\%$ . This is primarily caused by our veto band cuts which remove all simulated LAEs that happen to fall within a  $3\sigma$  isophote of a foreground source.

and  $y$ -band counterparts. We also base our  $1.8''$  color aperture corrections ( $-0.38$  and  $-0.32$  mag for WIDE12 and GAMA15A, respectively) on this profile when computing  $\text{Ly}\alpha$  fluxes for our LAE samples. This adopted Sérsic profile is similar to UV continuum profile measurements of LAE and LBG galaxies in the epoch of reionization (Jiang et al. 2013; Allen et al. 2017; Shibuya et al. 2019).

For our completeness simulations, the image positions of our artificial LAEs were randomly selected excluding regions flagged by our bright star mask (see Equation 3). To gain more statistical leverage at fainter fluxes, the simulated LAE NB fluxes,  $f_{\text{NB}}$ , were randomly sampled from a power law distribution ( $dN/df_{\text{NB}} \propto f_{\text{NB}}^{-2.5}$ ) with a minimum flux threshold of 26 mag. The  $y$ -band fluxes were assigned by randomly sampling an exponential EW distribution with a rest-frame scale length of  $100\text{\AA}$  and a minimum rest-frame EW threshold of  $5\text{\AA}$ . After inserting artificial sources, we performed our standard LAE selection and measured the fraction of all simulated EW  $> 10\text{\AA}$  objects successfully recovered, as a function of NB flux. This procedure allows us to correct for any EW incompleteness that is introduced by our  $2\Sigma$  and NB-excess cuts.

In Figure 6, we plot the recovered fraction of artificial sources as a function of total NB magnitude. We show the effect of sequentially applying our LAE selection cuts with the red, orange, green, and blue completeness curves. Our NB SNR cut removes faint LAEs not detected at  $5\sigma$  significance (red curve). Our NB-excess

cut removes LAEs with  $\text{EW} \lesssim 10\text{\AA}$  (orange curve). Our  $\Sigma$  parameter cut removes sources without a flux excess detected at  $2\sigma$  significance (green curve). This cut preferentially removes low-EW LAE candidates at faint NB magnitudes. Finally, our  $3\sigma$  veto band cuts remove simulated LAEs that are randomly positioned on the isophotes of foreground objects.

As discussed in detail by Hu et al. (2019) (see their discussion of “selection incompleteness”), even for NB bright LAEs we do not recover 100% of our inputted LAEs.

Both fields have a maximum total completeness of  $\sim 83\%$  as shown by the blue curve in Figure 6. This is mainly due to our veto band cuts that mask out any regions falling within the  $3\sigma$  isophotes of foreground sources. For both of our fields, we find that  $\sim 13\%$  of randomly placed  $D = 1.0''$  apertures have  $griz$ -band flux measurements above  $3\sigma$ . The remaining deficit ( $\sim 4\%$ ) is due to incomplete recovery of LAE candidates in the  $10\text{\AA} \lesssim \text{EW} \lesssim 20\text{\AA}$  range.

In Figure 6, we also show the NB magnitude distribution of our LAE candidates. The number of candidates rises with decreasing flux from the brightest LAEs in the field (at total AB magnitude NB964  $\sim 23$ ) to a peak at NB964  $\sim 24.4$ , indicating the rising luminosity function. Fainter than NB964  $\sim 24.5$ , it falls off with the declining completeness near the survey limit.

When calculating luminosity functions, we wish to reach the faintest fluxes where our data can provide useful measurements. In practice we select our complete-

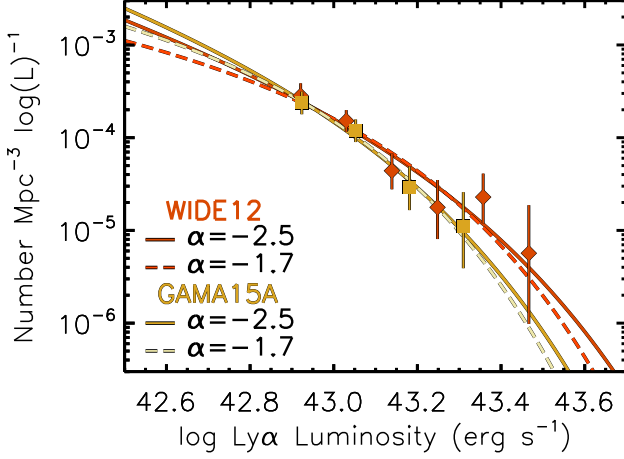


**Figure 7.** The LAGER WIDE12 (orange diamonds) and GAMA15A (yellow squares) Ly $\alpha$  LFs and best-fit Schechter functions. Field WIDE12 displays a more prominent bright-end ( $L_{\text{Ly}\alpha} > 10^{43.3} \text{ erg s}^{-1}$ ) tail compared to GAMA15A. An analogous result was also found between our two previous LAGER fields, COSMOS and CDFS, where COSMOS was found to have an over-dense bright-end.

ness threshold such that the bin-averaged completeness in our faintest luminosity function bins is  $\sim 25\%$ . This is comparable to other recent  $z \approx 7$  Ly $\alpha$  luminosity function studies (e.g., Ota et al. 2017 report a minimum binned completeness of  $\sim 22\%$  and  $\sim 35\%$  for their SDF and SXDS fields). We have therefore chosen to use all LAEs with individual completeness  $> 5\%$ , which yields bin-averaged completeness of 22% in the faintest bin of the WIDE12 luminosity function, and 30% in GAMA15A. This cut excludes 11 LAE candidates (5 in WIDE12, and 6 in GAMA15A), leaving us with a final sample size of  $N = 84$  LAEs that are used in luminosity function calculations in section 7. For all figures, tables, and analyses, we scale our Poisson LF error bars by our incompleteness.

## 7. LY $\alpha$ LUMINOSITY FUNCTIONS AT $Z = 6.9$

### 7.1. The WIDE12 and GAMA15A Ly $\alpha$ LFs

To explore field-to-field variations, we compute the WIDE12 and GAMA15A  $z = 6.94$  Ly $\alpha$  LF using the  $1/V_{\text{max}}$  technique (Felten 1976). In Figure 7, we show our  $\text{EW} > 10\text{\AA}$  Ly $\alpha$  luminosity function for both WIDE12 and GAMA15A. We find that WIDE12 displays a more prominent bright-end tail compared to GAMA15A. This is similar to what was found in our previous LAGER fields, where COSMOS was found to have a pronounced bright-end bump compared to CDFS. Applying a Kolmogorov-Smirnov test to the bright end LFs for the four fields ( $\log(L) > 43.04 \text{ erg/sec}$ ) confirms the COSMOS bright-end excess at confidence levels from

98% (compared to WIDE12) to 99.8% confidence (compared to GAMA15), while the bright end of the WIDE12 LF exceeds that of GAMA15 at the 95% level.

We fit a Schechter function (Schechter 1976) to our Ly $\alpha$  LF, where

$$\Phi(L)dL = \phi^* \left( \frac{L}{L^*} \right)^\alpha e^{-L/L^*} d\left( \frac{L}{L^*} \right). \quad (6)$$

Our data lack the faint luminosity range needed to constrain the faint-end slope, so we assume fixed values of  $\alpha = -2.5$  and  $\alpha = -1.7$  that are meant to encompass the viable range of high-redshift slopes. The  $\alpha = -2.5$  value is consistent with the best-fit values from NB Ly $\alpha$  surveys at  $z = 5.7$  and  $z = 6.6$  (Konno et al. 2018; Santos et al. 2016), while the  $\alpha = -1.7$  value is consistent with a deep spectroscopic survey at  $z = 5.7$  (Henry et al. 2012). Following Malhotra & Rhoads (2002), we fit our LFs and estimate parameter errors using Cash Statistics (Cash 1979). We report the best-fit  $\phi^*$  and  $L^*$  values and errors in Table 2.

To assess the amount of Ly $\alpha$  light emitted relative to other surveys we calculate the Ly $\alpha$  luminosity density,

$$\rho^{\text{Ly}\alpha} = \int L \Phi(L) dL. \quad (7)$$

We adopt integration limits of  $L_{\text{Ly}\alpha} = 10^{42.4} \text{ erg s}^{-1}$  to infinity which does not require large extrapolations to unobserved faint luminosities and is consistent with previous NB studies (Hu et al. 2019; Itoh et al. 2018; Konno et al. 2018). We list our luminosity density values and  $1\sigma$  errors in Table 2. We compute  $1\sigma$  errors with a Monte-Carlo simulation that perturbs our LF data by Poisson random deviates. This procedure is used to create  $N = 10,000$  perturbed LFs. We then perform our standard LF fitting and luminosity density calculation to find the inter-68-percentile of the resulting luminosity density distribution.

### 7.2. The 4-Field LAGER Ly $\alpha$ LF

The areas covered by the four LAGER fields are 3.24, 2.91, 1.90, and 2.14  $\text{deg}^2$  for WIDE12, GAMA15A, COSMOS, and CDFS, respectively. The corresponding survey volumes for Ly $\alpha$  galaxies at  $z = 6.9$  are 1.93, 1.73, 1.14, and  $1.29 \times 10^6 \text{ Mpc}^3$ , giving a total survey volume of  $6.1 \times 10^6 \text{ Mpc}^3$ . This is greater than a factor of  $\times 2$  larger than other  $z \sim 7$  Ly $\alpha$  LFs (see Table 3). In Figure 8, we show the WIDE12 and GAMA15A LAGER LFs compared to the COSMOS and CDFS LAGER LFs presented in Hu et al. (2019). The LF best-fit parameters are found to agree within their  $1\sigma$  Poisson errors, and we combine these data-sets to compute the 4-Field Ly $\alpha$  LF.

**Table 2.** Best-fit  $z = 6.9$  Ly $\alpha$  Luminosity Function Parameters

Field	$\log L_{\text{Ly}\alpha}$ Fitted Range ( $\text{erg s}^{-1}$ )	$\alpha$	$L^*$ ( $10^{42} \text{ erg s}^{-1}$ )	$\phi^*$ ( $10^{-4} \text{ Mpc}^{-3}$ )	$[\rho_{\text{Ly}\alpha}]_{42.4}^{\infty}$ ( $10^{39} \text{ erg s}^{-1} \text{ Mpc}^{-3}$ )	Displayed in
WIDE12	42.87-43.52	-2.5(fixed)	$9.31^{+7.79}_{-3.17}$	$2.24^{+5.98}_{-1.75}$	$2.71^{+0.81}_{-0.82}$	Figure 7, 8
	42.87-43.52	-1.7(fixed)	$6.03^{+2.60}_{-1.53}$	$5.20^{+8.13}_{-3.11}$	$2.03^{+0.55}_{-0.64}$	Figure 7
GAMA15A	42.86-43.37	-2.5(fixed)	$6.25^{+5.17}_{-2.16}$	$6.44^{+23.42}_{-5.34}$	$3.21^{+1.17}_{-0.99}$	Figure 7, 8
	42.86-43.37	-1.7(fixed)	$4.42^{+2.10}_{-1.13}$	$11.11^{+21.25}_{-7.43}$	$2.43^{+0.71}_{-0.85}$	Figure 7
WIDE12+	42.86-43.52	-2.5(fixed)	$7.05^{+2.77}_{-1.70}$	$4.52^{+6.44}_{-2.79}$	$2.98^{+0.64}_{-0.75}$	–
GAMA15A	42.86-43.52	-1.7(fixed)	$4.98^{+1.42}_{-0.95}$	$7.97^{+7.88}_{-3.98}$	$2.19^{+0.41}_{-0.59}$	–
LAGER 4F	42.69-43.54	-2.5(fixed)	$8.95^{+2.82}_{-1.79}$	$2.19^{+1.79}_{-1.09}$	$2.44^{+0.31}_{-0.36}$	Figure 9, 10
	42.69-43.54	-1.7(fixed)	$5.65^{+1.08}_{-0.87}$	$5.55^{+3.36}_{-1.88}$	$1.93^{+0.28}_{-0.27}$	Figure 9
	42.69-43.26	-2.5(fixed)	$5.92^{+1.94}_{-1.14}$	$6.99^{+7.47}_{-4.10}$	$3.07^{+0.41}_{-0.52}$	Figure 9
	42.69-43.26	-1.7(fixed)	$4.01^{+0.77}_{-0.61}$	$14.03^{+9.41}_{-5.81}$	$2.52^{+0.38}_{-0.37}$	Figure 9

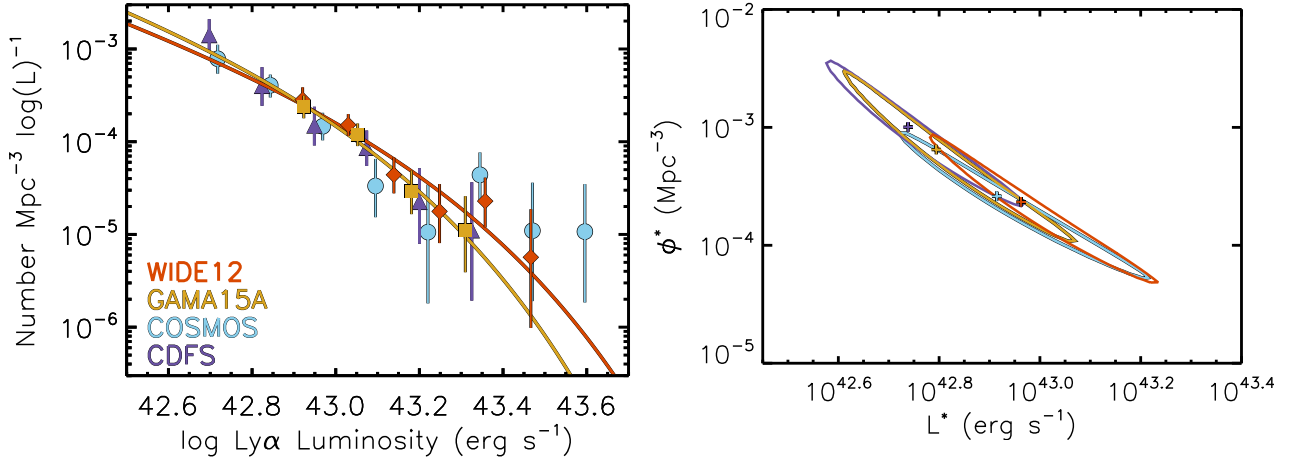


**Figure 8.** (Left) Individual LAGER field Ly $\alpha$  LFs (WIDE12: orange diamonds; GAMA15A: yellow squares; COSMOS: blue circles; CDFS: purple triangles). The best-fit Schechter functions are shown for fields WIDE12 and GAMA15A. (Right) Corresponding  $1\sigma$  confidence intervals of the best-fit Schechter parameters for all four LAGER fields. For the Schechter functions and corresponding confidence contours, we assume a fixed faint-end slope of  $\alpha = -2.5$ . We find good  $1\sigma$  agreement between all LAGER fields.

In Figure 9, we show the 4-Field LAGER LF and our 1 and  $2\sigma$  confidence contours. We again see evidence in this LF for a bright-end bump, and we illustrate the effect of excluding the brightest luminosities data points ( $L_{\text{Ly}\alpha} > 10^{43.3} \text{ erg s}^{-1}$ ) from our Schechter function fit in Figure 9. We list all of our best-fit Ly $\alpha$  LF parameters in Table 2. We find that our fit with a steep faint-end slope of  $\alpha = -2.5$  is a marginally better description of our Ly $\alpha$  data points. However, if the bright-end bump is excluded in the fits, then the distinction between faint-end slopes largely goes away.

## 8. DISCUSSION

### 8.1. The Ly $\alpha$ IGM Transmission Fraction and the Neutral Hydrogen Fraction

In Table 3 and Figure 10, we show how our  $z = 6.9$  4-Field LAGER Ly $\alpha$  LF compares to other high-redshift LFs. We note that factor of  $\sim 2$  discrepancies between Ly $\alpha$  LFs at the same redshift are found between different NB surveys. While some of this variation can be attributed to field-to-field variation, survey systematics likely play a role (e.g., see the discussion in Taylor et al. 2020).

To measure the Ly $\alpha$  IGM transmission fraction at  $z = 6.9$ , we need to compare our Ly $\alpha$  LF to a reference LF that is at a low enough redshift to be outside the reionization epoch, yet in close redshift proximity to minimize any evolution of the LAE galaxy population. We know from  $z \sim 6$  quasar spectra that the reionization of the IGM is largely complete at  $z \sim 6$  (Fan et al.

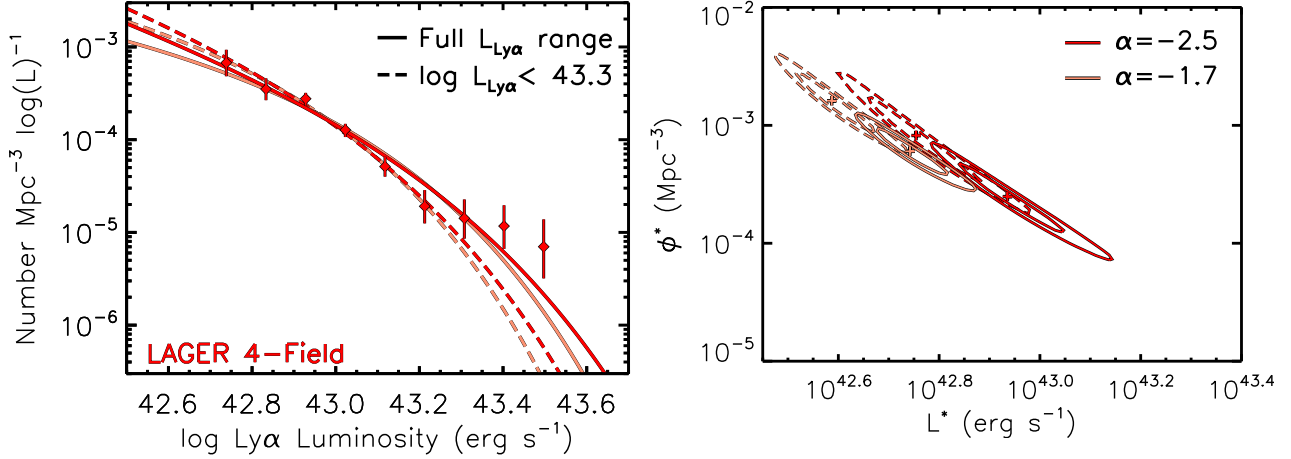


**Figure 9.** (Left) The combined LAGER 4-Field Ly $\alpha$  LF and best-fit Schechter functions. (Right) Corresponding 1 and 2 $\sigma$  confidence intervals for the best-fit Schechter parameters.

2006). Thus, we compare our sample to the  $z = 5.7$  Ly $\alpha$  sample from Konno et al. (2018), and we are particularly interested in accounting for any systematic uncertainties between these surveys. Before computing the Ly $\alpha$  IGM transmission fraction and neutral hydrogen fraction, we consider the importance of systematics introduced by Ly $\alpha$  survey EW limits and selection completeness.

#### 8.1.1. Ly $\alpha$ Survey EW Limits

We show in Table 3 that archival surveys have adopted different EW limits when computing their Ly $\alpha$  LFs. The EW limits listed in Table 3 have been re-computed in a consistent manner so that relative comparisons can be made. Following the procedure we used for our LAGER Ly $\alpha$  flux measurements (see Section 4), we assume the LAE candidates have a delta-function Ly $\alpha$  line profile at the center of the NB filter and a UV continuum slope of  $-2$  that is attenuated by the IGM via the Inoue et al. (2014) model. Given this assumed spectral shape, the NB/BB filter responses, and the study-specific NB-excess cut, we compute the survey’s EW limit.

To estimate the importance of the EW selection difference, we consider a non-evolving EW distribution parameterized by a declining exponential and a scale length of  $100 \text{ \AA}$ . Given the extremes of the EW lower-limits shown in Table 3, we estimate that the different EW limits could at most account for a factor of  $\sim 1.6$  number density variations. In general, we find that the survey-to-survey variation introduced by this variation should be relatively small with the caveat that we have not considered an evolving EW scale length with redshift or other scale length dependencies. Using the same methodology, we specifically compare our  $\text{EW} > 10 \text{ \AA}$  survey at  $z = 6.9$  to Konno et al.’s  $\text{EW} > 4 \text{ \AA}$  survey at  $z = 5.7$ . We find that if their survey

adopted an  $\text{EW} > 10 \text{ \AA}$  cut, their Ly $\alpha$  number density would decline by a small factor of  $\sim 1.06$ .

#### 8.1.2. Selection Completeness

Recently, another source of systematic error was emphasized by Hu et al. (2019), selection completeness. They found that high-redshift NB surveys can lose a significant fraction of their survey area by requiring non-detections in all of their veto bandpasses. However, this effect is not accounted for in the high-redshift NB surveys that we compare to and show in Figure 10. The size of the area lost to this effect depends on several variables including veto band depth, seeing, extraction aperture size, and the scope of the applied bright star mask, and it is unlikely to be constant between surveys. For example, Hu et al. (2019) found that about 40% of their survey area is masked by  $3\sigma$  veto sources. While for our WIDE12 and GAMA15A fields with shallower veto bandpasses, we find that only  $\sim 15\%$  of our survey area is masked. By accounting for this incompleteness, we compute accurate survey areas and find luminosity densities that are consistent within  $1\sigma$  between our combined WIDE12+GAMA15A and the combined COSMOS+CDFS measurements.

The  $z = 5.7$  NB Ly $\alpha$  LFs do not account for selection incompleteness, so we quantify this effect, which - if left unaccounted for - will cause an over-estimate of the survey’s area and a corresponding under-estimate of the LF’s normalization,  $\phi^*$  (see Hu et al. 2019, for details). Konno et al. use the deeper  $z = 5.7$  Ly $\alpha$  survey from Ouchi et al. (2008) to constrain the faint-end of their LF fit. Their resulting combined fit to these two different data-sets with different veto-band depths makes it difficult to estimate an effective selection incompleteness. To simplify the problem, we re-fit Konno et al.’s  $z = 5.7$  Ly $\alpha$  LF assuming a fixed faint-end slope

**Table 3.** Comparison of high-redshift LAE surveys. The lower-limit  $EW_{Ly\alpha}^{\text{lim}}$  are computed with the survey’s NB excess criteria and corresponding NB and BB filters but normalized to a common assumed LAE spectrum and IGM attenuation prescription as described in section 8.1.1.

Reference	Redshift	Cosmic Age (Gyr)	Volume (Mpc <sup>3</sup> )	$EW_{Ly\alpha}^{\text{lim}}$ (Å)	$\log L_{Ly\alpha}^{\text{lim}}$ log (erg s <sup>-1</sup> )	Figure 10 symbol
This work	6.93	0.76	$6.1 \times 10^6$	10	42.7	red diamond
Herenz et al. (2019)	5.0-6.7	1.15-0.79	$2.3 \times 10^5$	—	42.2	blue circle
Drake et al. (2017)	5.0-6.6	1.15-0.81	$3.6 \times 10^4$	—	41.0	blue square
Santos et al. (2016)	5.7	0.98	$6.3 \times 10^6$	6	42.5	purple triangle
Konno et al. (2018)	5.7	0.98	$1.2 \times 10^7$	4	42.9	purple circle
Ouchi et al. (2008)	5.7	0.98	$9.2 \times 10^5$	6	42.5	purple square
Matthee et al. (2015)	6.6	0.81	$4.3 \times 10^6$	48	42.5	green triangle
Konno et al. (2018)	6.6	0.81	$1.9 \times 10^7$	15	43.0	green circle
Ouchi et al. (2010)	6.6	0.81	$8.0 \times 10^5$	48	42.4	green square
Itoh et al. (2018)	6.99	0.75	$2.2 \times 10^6$	12	42.9	red circle
Ota et al. (2017)	7.02	0.75	$6.1 \times 10^5$	0	42.6	red square
Konno et al. (2014)	7.30	0.71	$2.5 \times 10^5$	0	42.4	grey circle
Shibuya et al. (2012)	7.27	0.71	$5.9 \times 10^5$	0	42.7	grey square

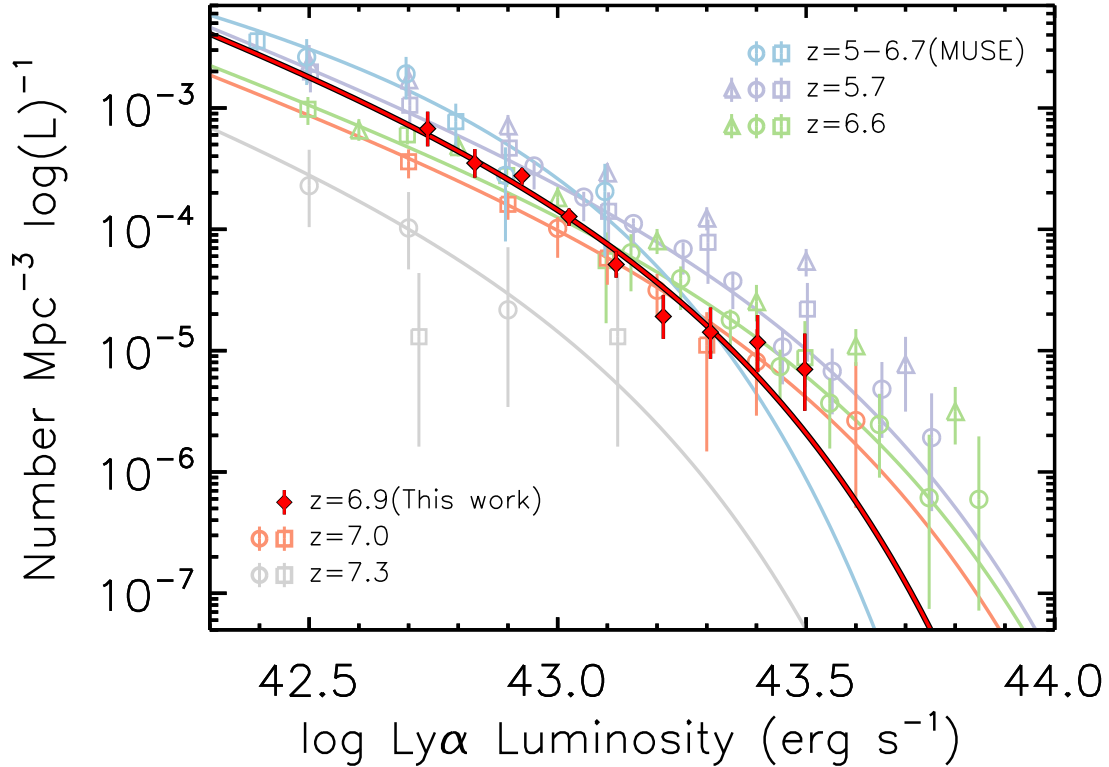


**Figure 10.** The combined  $z = 6.9$  LAGER 4-Field  $Ly\alpha$  LF compared to archival studies. We list the displayed archival references and corresponding point symbols in Table 3. We show the best-fit  $z = 5.7, 6.6,$  and  $7.3$  Schechter functions with  $\alpha \sim -2.5$  as compiled in Itoh et al. (2018). We also show the best-fit  $3 > z > 6.7$  MUSE-Wide  $Ly\alpha$  LF with  $\alpha = -1.84$  from Herenz et al. (2019). Within the luminosity range probed by MUSE-Wide, this  $3 > z > 6.7$  LF was found to be consistent with their highest redshift  $Ly\alpha$  LF at  $5 > z > 6.7$  (shown by open blue circles).



of  $\alpha = -2.5$  but without the Ouchi et al. data. We compute a Ly $\alpha$  luminosity density of  $3.70 \times 10^{39} \text{ erg s}^{-1} \text{ Mpc}^{-3}$  which is within  $1\sigma$  of the published  $z = 5.7$  result ( $3.49^{+0.58}_{-0.71} \times 10^{39} \text{ erg s}^{-1} \text{ Mpc}^{-3}$  Konno et al. 2018; Itoh et al. 2018).

Konno et al. use HSC-SSP internal data release S16A  $g$ -band images to construct their  $g > g_{3\sigma}$  veto-band selection over four fields: COSMOS, SXDS, DEEP2-3, and ELAIS-N1. The publicly available dataset with the closest image characteristics to S16A is HSC-SSP DR1, and we use a  $0.5 \times 0.5 \text{ deg}^2$  HSC-SSP DR1 COSMOS  $g$ -band image in the UltraDeep layer to characterize their veto-band selection completeness. We randomly place  $N = 10,000$   $D = 1.5''$  apertures in our DR1  $g$ -band sub-image and find that 16% of these random apertures would not be selected due to overlap with  $3\sigma$  isophotes of foreground objects. However, Konno et al. apply a bright star mask that removes  $\sim 7\%$  of the survey area within our sub-field (Coupon et al. 2018), implying a final selection incompleteness of  $\sim 9\%$ . Correcting for this estimated selection incompleteness and the different EW limits, we compute a  $z = 5.7$  Ly $\alpha$  luminosity density of  $3.84^{+0.64}_{-0.71} \times 10^{39} \text{ erg s}^{-1} \text{ Mpc}^{-3}$ . The overall correction that we apply is small and simply using Konno et al.’s published luminosity density value would not significantly alter our results.

### 8.1.3. Ly $\alpha$ IGM Transmission Fraction

We compute the Ly $\alpha$  IGM transmission fraction via:

$$\frac{T_{z=6.9}^{\text{IGM}}}{T_{z=5.7}^{\text{IGM}}} = \frac{\rho_{z=6.9}^{\text{Ly}\alpha} / \rho_{z=5.7}^{\text{Ly}\alpha}}{\rho_{z=6.9}^{\text{UV}} / \rho_{z=5.7}^{\text{UV}}} = 1.0^{+0.26}_{-0.28}, \quad (8)$$

which assumes unchanging ISM properties and stellar populations from  $z = 5.7$  to  $6.9$ , a 200 Myr duration (see also Zheng et al. 2017; Konno et al. 2018; Itoh et al. 2018; Hu et al. 2019, for a similar procedure). We use the corrected  $z = 5.7$  Ly $\alpha$  luminosity density of  $3.84 \times 10^{39} \text{ erg s}^{-1} \text{ Mpc}^{-3}$  and our  $z = 6.9$  4-Field LAGER Ly $\alpha$  luminosity density of  $2.44 \times 10^{39} \text{ erg s}^{-1} \text{ Mpc}^{-3}$ . These luminosity densities are computed with consistent integration limits and a fixed faint-end slope of  $\alpha = -2.5$ . We compute a Ly $\alpha$  luminosity density ratio of  $\rho_{z=6.9}^{\text{Ly}\alpha} / \rho_{z=5.7}^{\text{Ly}\alpha} = 0.63^{+0.13}_{-0.15}$  and use the UV ratio of  $\rho_{z=6.9}^{\text{UV}} / \rho_{z=5.7}^{\text{UV}} = 0.63 \pm 0.09$  from Finkelstein et al. (2015). These ratios are consistent with the UV and Ly $\alpha$  LF’s evolving at a similar rate from  $z = 5.7$  to  $6.9$  and imply a Ly $\alpha$  IGM transmission fraction of  $T_{z=6.9}^{\text{IGM}} / T_{z=5.7}^{\text{IGM}} = 1.0^{+0.26}_{-0.28}$ .

### 8.1.4. Volume-Averaged Neutral Hydrogen Fraction

The conversion of Ly $\alpha$  transmission fractions to a neutral hydrogen fraction  $x_{\text{HI}}$  is model dependent. By

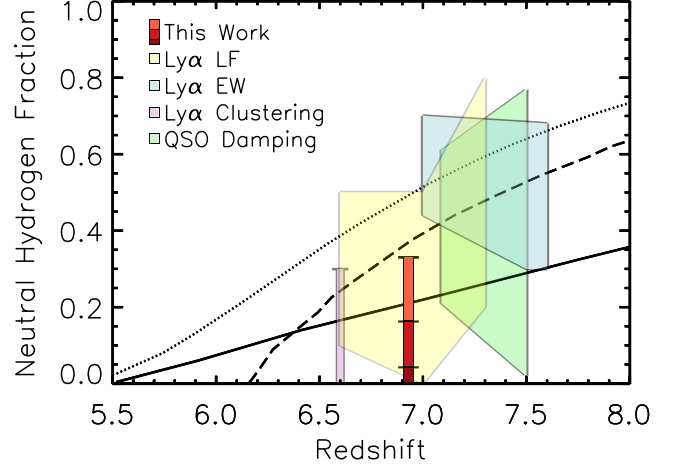


**Figure 11.** Evolution of the volume-averaged  $x_{\text{HI}}$ . Our  $1\sigma$  upper limit results based on three different Ly $\alpha$  transmission models (red shaded bars, see Table 4 and Section 8.1.4 for details) are shown relative to other observational constraints. While we adopt the most conservative limit of  $x_{\text{HI}} < 0.33$  at  $z = 6.9$ , we show the more restrictive constraints favored by alternative reionization models with different shading. Our observational constraint favors the more gradual reionization scenario proposed by Finkelstein et al. (2019, solid curve) while being at odds with the late and rapid reionization scenario presented by Robertson et al. (2015, dashed curve) and Kulkarni et al. (2019, dotted curve). The displayed regions show the parameter space allowed by the  $\pm 1\sigma$  results from archival studies. The Ly $\alpha$  LF region is defined by the results from Konno et al. (2018), Itoh et al. (2018), Konno et al. (2014), and Inoue et al. (2018). The Ly $\alpha$  EW region is defined by the results from Mason et al. (2018), Tilvi et al. (2014), and Jung et al. (2020). The Ly $\alpha$  clustering region is defined by the results from Ouchi et al. (2018). The QSO damping region is defined by the results from Greig et al. (2017), Greig et al. (2019), and Bañados et al. (2018).

employing multiple theoretical models, we quantify systematic errors. All of the following  $x_{\text{HI}}$  estimates are volume-averaged neutral hydrogen fractions.

First, we use our Ly $\alpha$  LF to constrain the radiative transfer simulations of McQuinn et al. (2007) which display the expected drop in the cumulative Ly $\alpha$  LF in their Figure 5. Taking the  $1\sigma$  lower bound on transmission ( $T_{-1\sigma} = 0.72$ ), this figure implies upper limits of  $x_{\text{HI}} < 0.16$ ,  $x_{\text{HI}} < 0.33$ , and  $x_{\text{HI}} < 0.11$ , respectively, for McQuinn et al. (2007)’s models I, II, and III. The models differ in their assumed scaling of ionizing photon production with halo mass. Model I is a straight proportionality, while model II gives greater weight to the most massive halos ( $\dot{N}_{\text{ion}} \propto M^{5/3}$ ), resulting in larger bubbles and corresponding qualitatively to the recent “oligarchs” model (Naidu et al. 2020). Model III has yet smaller bubbles due to minihalo absorption of Lyman continuum photons.

**Table 4.** IGM neutral hydrogen fraction constraints.

Reference and Relevant Figures	Observational Constraints	Model $x_{\text{HI}}$ at $z = 6.9$
Malhotra & Rhoads (2006) Fig.1 & 2	$T^{\text{IGM}}$ & Ly $\alpha$ number density	0.00 – 0.04
Dijkstra et al. (2007) Fig.6 & Furlanetto et al. (2006) Fig.1	$T^{\text{IGM}}$	0.00 – 0.16
McQuinn et al. (2007) Fig.5	cumulative Ly $\alpha$ LF	0.00 – 0.33

We also estimate the  $z = 6.9$  neutral hydrogen fraction with a Ly $\alpha$  volume test where each observed LAE is taken as evidence for an ionized bubble allowing for Ly $\alpha$  escape (Malhotra & Rhoads 2006). Using  $T_{z=6.9}^{\text{IGM}}/T_{z=5.7}^{\text{IGM}} = 1.0^{+0.26}_{-0.28}$ , a Ly $\alpha$  velocity shift of  $200 - 300 \text{ km s}^{-1}$  (e.g., McLinden et al. 2011), a correlation length of 4 Mpc, and a Ly $\alpha$  number density of  $\sim 1.5 \times 10^{-4} \text{ Mpc}^{-3}$ , we find  $x_{\text{HI}} < 0.04$  via Malhotra & Rhoads (2006, Figure 1 and 2).

Finally, we use the analytical models of Dijkstra et al. (2007) and Furlanetto et al. (2006) to estimate the typical size of ionized bubbles and then use this value to constrain the neutral hydrogen fraction to be  $x_{\text{HI}} < 0.16$ . We summarize all of the  $x_{\text{HI}}$  constraints in Table 4.

Adopting a conservative limit, we conclude that  $x_{\text{HI}} < 0.33$  at  $z = 6.9$ . In Figure 11, we show our  $z = 6.9$  constraint in comparison to model predictions and other observational constraints. Our  $x_{\text{HI}}$  estimate is consistent with other results based on Ly $\alpha$  LFs (Konno et al. 2014, 2018; Itoh et al. 2018; Inoue et al. 2018), Ly $\alpha$  clustering (Ouchi et al. 2018), Ly $\alpha$  EW tests (Mason et al. 2018; Tilvi et al. 2014; Jung et al. 2020), and QSO damping wings (Greig et al. 2017; Bañados et al. 2018; Greig et al. 2019). Our observational constraint favors the more gradual reionization scenario proposed by Finkelstein et al. (2019) but is in tension with a rapid reionization scenario preferred by Robertson et al. (2015) and Kulkarni et al. (2019).

With the conclusion of LAGER we will more than double our current survey area enabling us to further constrain  $x_{\text{HI}}$  based on Ly $\alpha$  LF tests. Additionally, the increased Ly $\alpha$  sample size will allow us to conduct Ly $\alpha$  clustering analyses which will give us another handle on the  $z = 6.9$  hydrogen neutral fraction.

## 9. SUMMARY

We present the LAGER 4-Field  $z = 6.9$  Ly $\alpha$  luminosity function. We identified  $N = 95$  new Ly $\alpha$  emitters selected in the WIDE12 and GAMA15A fields and combine this sample with the existing COSMOS and CDFS LAGER Ly $\alpha$  sample. We compute the 4-Field LAGER Ly $\alpha$  luminosity function with a survey volume of  $6.1 \times 10^6 \text{ Mpc}^3$ . This is more than double the size of

the next largest  $z \sim 7$  Ly $\alpha$  survey. We investigate potential systematics in NB Ly $\alpha$  surveys and taking these issues into account we estimate a Ly $\alpha$  IGM transmission of  $T_{z=6.9}^{\text{IGM}}/T_{z=5.7}^{\text{IGM}} = 1.0^{+0.26}_{-0.28}$  which is consistent with a fully ionized  $z = 6.9$  neutral hydrogen fraction. Using our  $1\sigma$  lower bound on transmission ( $T_{-1\sigma} = 0.72$ ), we find that the most conservative reionization model predicts a volume-averaged neutral hydrogen fraction of  $x_{\text{HI}} < 0.33$ .

## ACKNOWLEDGMENTS

We thank the anonymous referee for comments that substantially improved the manuscript. IGBW is supported by an appointment to the NASA Postdoctoral Program at the Goddard Space Flight Center, administered by the Universities Space Research Association through a contract with NASA. The material is based upon work supported by NASA under award number 80GSFC21M0002. The LAGER survey has been supported in part by the US National Science Foundation through NSF grant AST-1518057.

This work was funded by ANID projects CATABASAL AFB-170002 (L.F.B., F.E.B.), FONDECYT Regular 1190818 (F.E.B.) and 1200495 (F.E.B.), and Millennium Science Initiative Program ICN12.009 (F.E.B.).

J.X.W. and W.D.H are supported by National Science Foundation of China (grants No. 11421303 & 11890693) and CAS Frontier Science Key Research Program (QYZDJ-SSW-SLH006). Z.Y.Z. thanks the National Science Foundation of China (11773051, 12022303) and the CAS Pioneer Hundred Talents Program.

## ACKNOWLEDGMENTS

This project used data obtained with the Dark Energy Camera (DECam), which was constructed by the Dark Energy Survey (DES) collaboration. Funding for the DES Projects has been provided by the U.S. Department of Energy, the U.S. National Science Foundation, the Ministry of Science and Education of Spain, the Science and Technology Facilities Council of the United Kingdom, the Higher Education Funding Council for England, the National Center for Supercomputing Applications at the University of Illinois at Urbana-Champaign, the Kavli Institute of Cosmological Physics at the University of Chicago, Center for Cosmology and Astro-Particle Physics at the Ohio State University, the Mitchell Institute for Fundamental Physics and Astronomy at Texas A&M University, Financiadora de Estudos e Projetos, Fundação Carlos Chagas Filho de Amparo, Financiadora de Estudos e Projetos, Fundação Carlos Chagas Filho de Amparo à Pesquisa do Estado do Rio de Janeiro, Conselho Nacional de Desenvolvimento Científico e Tecnológico and the Ministério da Ciência, Tecnologia e Inovação, the Deutsche Forschungsgemeinschaft and the Collaborating Institutions in the Dark Energy Survey.

The Collaborating Institutions are Argonne National Laboratory, the University of California at Santa Cruz, the University of Cambridge, Centro de Investigaciones Energéticas, Medioambientales y Tecnológicas-Madrid, the University of Chicago, University College London, the DES-Brazil Consortium, the University of Edinburgh, the Eidgenössische Technische Hochschule (ETH) Zürich, Fermi National Accelerator Laboratory, the University of Illinois at Urbana-Champaign, the Institut de Ciències de l'Espai (IEEC/CSIC), the Institut de Física d'Altes Energies, Lawrence Berkeley National Laboratory, the Ludwig-Maximilians Universität München and the associated Excellence Cluster Universe, the University of Michigan, the National Optical Astronomy Observatory, the University of Nottingham, the Ohio State University, the OzDES Membership Consortium, the University of Pennsylvania, the University of Portsmouth, SLAC National Accelerator Laboratory, Stanford University, the University of Sussex, and Texas A&M University.

Based on observations at Cerro Tololo Inter-American Observatory, NSF–NOIRLab (NOIRLab Prop. ID 2017A-0366, 2018A-0371, 2018B-0327; PI: S. Malhotra; 2018B-0907, 2019A-0912; PI: L. F. Barrientos; 2017A-0920; PI: L. Infante), which is operated by the Association of Universities for Research in Astronomy (AURA) under a cooperative agreement with the National Science Foundation.

## ACKNOWLEDGMENTS

The Hyper Suprime-Cam (HSC) collaboration includes the astronomical communities of Japan and Taiwan, and Princeton University. The HSC instrumentation and software were developed by the National Astronomical Observatory of Japan (NAOJ), the Kavli Institute for the Physics and Mathematics of the Universe (Kavli IPMU), the University of Tokyo, the High Energy Accelerator Research Organization (KEK), the Academia Sinica Institute for Astronomy and Astrophysics in Taiwan (ASIAA), and Princeton University. Funding was contributed by the FIRST program from Japanese Cabinet Office, the Ministry of Education, Culture, Sports, Science and Technology (MEXT), the Japan Society for the Promotion of Science (JSPS), Japan Science and Technology Agency (JST), the Toray Science Foundation, NAOJ, Kavli IPMU, KEK, ASIAA, and Princeton University.

This paper makes use of software developed for the Large Synoptic Survey Telescope. We thank the LSST Project for making their code available as free software at <http://dm.lsst.org>

This paper is based in part on data collected at the Subaru Telescope and retrieved from the HSC data archive system, which is operated by Subaru Telescope and Astronomy Data Center at National Astronomical Observatory of Japan. Data analysis was in part carried out with the cooperation of Center for Computational Astrophysics, National Astronomical Observatory of Japan.

This publication makes use of data products from the Two Micron All Sky Survey, which is a joint project of the University of Massachusetts and the Infrared Processing and Analysis Center/California Institute of Technology, funded by the National Aeronautics and Space Administration and the National Science Foundation.

The Pan-STARRS1 Surveys (PS1) and the PS1 public science archive have been made possible through contributions by the Institute for Astronomy, the University of Hawaii, the Pan-STARRS Project Office, the Max-Planck Society and its participating institutes, the Max Planck Institute for Astronomy, Heidelberg and the Max Planck Institute for Extraterrestrial Physics, Garching, The Johns Hopkins University, Durham University, the University of Edinburgh, the Queen's University Belfast, the Harvard-Smithsonian Center for Astrophysics, the Las Cumbres Observatory Global Telescope Network Incorporated, the National Central University of Taiwan, the Space Telescope Science Institute, the National Aeronautics and Space Administration under Grant No. NNX08AR22G issued through the Planetary Science Division of the NASA Science Mission Directorate, the National Science Foundation Grant No. AST-1238877, the University of Maryland, Eotvos Lorand University (ELTE), the Los Alamos National Laboratory, and the Gordon and Betty Moore Foundation.

## REFERENCES

- Aihara, H., Arimoto, N., Armstrong, R., et al. 2018, PASJ, 70, S4, doi: [10.1093/pasj/psx066](https://doi.org/10.1093/pasj/psx066)
- Allen, R. J., Kacprzak, G. G., Glazebrook, K., et al. 2017, ApJL, 834, L11, doi: [10.3847/2041-8213/834/2/L11](https://doi.org/10.3847/2041-8213/834/2/L11)
- Bañados, E., Venemans, B. P., Mazzucchelli, C., et al. 2018, Nature, 553, 473, doi: [10.1038/nature25180](https://doi.org/10.1038/nature25180)
- Bertin, E., & Arnouts, S. 1996, A&AS, 117, 393
- Bertin, E., Mellier, Y., Radovich, M., et al. 2002, in Astronomical Society of the Pacific Conference Series, Vol. 281, Astronomical Data Analysis Software and Systems XI, ed. D. A. Bohlender, D. Durand, & T. H. Handley, 228
- Blanc, G. A., Adams, J. J., Gebhardt, K., et al. 2011, ApJ, 736, 31, doi: [10.1088/0004-637X/736/1/31](https://doi.org/10.1088/0004-637X/736/1/31)
- Bosch, J., Armstrong, R., Bickerton, S., et al. 2018, PASJ, 70, S5, doi: [10.1093/pasj/psx080](https://doi.org/10.1093/pasj/psx080)
- Bouwens, R. J., Illingworth, G. D., Oesch, P. A., et al. 2015, ApJ, 803, 34, doi: [10.1088/0004-637X/803/1/34](https://doi.org/10.1088/0004-637X/803/1/34)
- Bunker, A. J., Warren, S. J., Hewett, P. C., & Clements, D. L. 1995, MNRAS, 273, 513, doi: [10.1093/mnras/273.2.513](https://doi.org/10.1093/mnras/273.2.513)
- Cash, W. 1979, ApJ, 228, 939, doi: [10.1086/156922](https://doi.org/10.1086/156922)
- Chambers, K. C., Magnier, E. A., Metcalfe, N., et al. 2016, arXiv e-prints, arXiv:1612.05560. <https://arxiv.org/abs/1612.05560>
- Coughlin, A., Rhoads, J. E., Malhotra, S., et al. 2018, ApJ, 858, 96, doi: [10.3847/1538-4357/aab620](https://doi.org/10.3847/1538-4357/aab620)
- Coupon, J., Czakon, N., Bosch, J., et al. 2018, PASJ, 70, S7, doi: [10.1093/pasj/psx047](https://doi.org/10.1093/pasj/psx047)
- Cowie, L. L., Barger, A. J., & Hu, E. M. 2011, ApJ, 738, 136, doi: [10.1088/0004-637X/738/2/136](https://doi.org/10.1088/0004-637X/738/2/136)
- Cowie, L. L., & Hu, E. M. 1998, AJ, 115, 1319, doi: [10.1086/300309](https://doi.org/10.1086/300309)
- Cutri, R. M., Skrutskie, M. F., van Dyk, S., et al. 2003, 2MASS All Sky Catalog of point sources.
- Deharveng, J.-M., Small, T., Barlow, T. A., et al. 2008, ApJ, 680, 1072, doi: [10.1086/587953](https://doi.org/10.1086/587953)
- Dijkstra, M., Wyithe, J. S. B., & Haiman, Z. 2007, MNRAS, 379, 253, doi: [10.1111/j.1365-2966.2007.11936.x](https://doi.org/10.1111/j.1365-2966.2007.11936.x)
- Drake, A. B., Garel, T., Wisotzki, L., et al. 2017, A&A, 608, A6, doi: [10.1051/0004-6361/201731431](https://doi.org/10.1051/0004-6361/201731431)
- Fan, X., Strauss, M. A., Becker, R. H., et al. 2006, AJ, 132, 117, doi: [10.1086/504836](https://doi.org/10.1086/504836)
- Felten, J. E. 1976, ApJ, 207, 700, doi: [10.1086/154538](https://doi.org/10.1086/154538)
- Finkelstein, S. L., Papovich, C., Dickinson, M., et al. 2013, Nature, 502, 524, doi: [10.1038/nature12657](https://doi.org/10.1038/nature12657)
- Finkelstein, S. L., Ryan, Russell E., J., Papovich, C., et al. 2015, ApJ, 810, 71, doi: [10.1088/0004-637X/810/1/71](https://doi.org/10.1088/0004-637X/810/1/71)
- Finkelstein, S. L., D'Aloisio, A., Paardekoooper, J.-P., et al. 2019, ApJ, 879, 36, doi: [10.3847/1538-4357/ab1ea8](https://doi.org/10.3847/1538-4357/ab1ea8)
- Furlanetto, S. R., Zaldarriaga, M., & Hernquist, L. 2006, MNRAS, 365, 1012, doi: [10.1111/j.1365-2966.2005.09785.x](https://doi.org/10.1111/j.1365-2966.2005.09785.x)
- Gawiser, E., van Dokkum, P. G., Herrera, D., et al. 2006, ApJS, 162, 1, doi: [10.1086/497644](https://doi.org/10.1086/497644)
- Gawiser, E., Francke, H., Lai, K., et al. 2007, ApJ, 671, 278, doi: [10.1086/522955](https://doi.org/10.1086/522955)
- Greig, B., Mesinger, A., & Bañados, E. 2019, MNRAS, 484, 5094, doi: [10.1093/mnras/stz230](https://doi.org/10.1093/mnras/stz230)
- Greig, B., Mesinger, A., Haiman, Z., & Simcoe, R. A. 2017, MNRAS, 466, 4239, doi: [10.1093/mnras/stw3351](https://doi.org/10.1093/mnras/stw3351)
- Gronwall, C., Ciardullo, R., Hickey, T., et al. 2007, ApJ, 667, 79, doi: [10.1086/520324](https://doi.org/10.1086/520324)
- Gruen, D., Seitz, S., & Bernstein, G. M. 2014, PASP, 126, 158, doi: [10.1086/675080](https://doi.org/10.1086/675080)
- Harish, S., Wold, I. G. B., Malhotra, S., et al. 2021, arXiv e-prints, arXiv:2111.01173. <https://arxiv.org/abs/2111.01173>
- Henry, A. L., Martin, C. L., Dressler, A., Sawicki, M., & McCarthy, P. 2012, ApJ, 744, 149, doi: [10.1088/0004-637X/744/2/149](https://doi.org/10.1088/0004-637X/744/2/149)
- Herenz, E. C., Wisotzki, L., Saust, R., et al. 2019, A&A, 621, A107, doi: [10.1051/0004-6361/201834164](https://doi.org/10.1051/0004-6361/201834164)
- Hu, E. M., Cowie, L. L., Barger, A. J., et al. 2010, ApJ, 725, 394, doi: [10.1088/0004-637X/725/1/394](https://doi.org/10.1088/0004-637X/725/1/394)
- Hu, E. M., Cowie, L. L., & McMahon, R. G. 1998, ApJL, 502, L99, doi: [10.1086/311506](https://doi.org/10.1086/311506)
- Hu, W., Wang, J., Zheng, Z.-Y., et al. 2017, ApJL, 845, L16, doi: [10.3847/2041-8213/aa8401](https://doi.org/10.3847/2041-8213/aa8401)
- . 2019, arXiv e-prints, arXiv:1903.09046. <https://arxiv.org/abs/1903.09046>
- Hu, W., Wang, J., Infante, L., et al. 2021, Nature Astronomy, doi: [10.1038/s41550-020-01291-y](https://doi.org/10.1038/s41550-020-01291-y)
- Inoue, A. K., Shimizu, I., Iwata, I., & Tanaka, M. 2014, MNRAS, 442, 1805, doi: [10.1093/mnras/stu936](https://doi.org/10.1093/mnras/stu936)
- Inoue, A. K., Hasegawa, K., Ishiyama, T., et al. 2018, PASJ, 70, 55, doi: [10.1093/pasj/psy048](https://doi.org/10.1093/pasj/psy048)
- Itoh, R., Ouchi, M., Zhang, H., et al. 2018, ApJ, 867, 46, doi: [10.3847/1538-4357/aadfe4](https://doi.org/10.3847/1538-4357/aadfe4)
- Jensen, H., Hayes, M., Iliev, I. T., et al. 2014, MNRAS, 444, 2114, doi: [10.1093/mnras/stu1600](https://doi.org/10.1093/mnras/stu1600)
- Jiang, L., Egami, E., Mechtley, M., et al. 2013, ApJ, 772, 99, doi: [10.1088/0004-637X/772/2/99](https://doi.org/10.1088/0004-637X/772/2/99)
- Jung, I., Finkelstein, S. L., Dickinson, M., et al. 2020, ApJ, 904, 144, doi: [10.3847/1538-4357/abbd44](https://doi.org/10.3847/1538-4357/abbd44)

- Keenan, R. C., Trouille, L., Barger, A. J., Cowie, L. L., & Wang, W.-H. 2010, *ApJS*, 186, 94, doi: [10.1088/0067-0049/186/1/94](https://doi.org/10.1088/0067-0049/186/1/94)
- Khostovan, A. A., Malhotra, S., Rhoads, J. E., et al. 2020, *MNRAS*, 171, doi: [10.1093/mnras/staa175](https://doi.org/10.1093/mnras/staa175)
- Konno, A., Ouchi, M., Nakajima, K., et al. 2016, *ApJ*, 823, 20, doi: [10.3847/0004-637X/823/1/20](https://doi.org/10.3847/0004-637X/823/1/20)
- Konno, A., Ouchi, M., Ono, Y., et al. 2014, *ApJ*, 797, 16, doi: [10.1088/0004-637X/797/1/16](https://doi.org/10.1088/0004-637X/797/1/16)
- Konno, A., Ouchi, M., Shibuya, T., et al. 2018, *PASJ*, 70, S16, doi: [10.1093/pasj/psx131](https://doi.org/10.1093/pasj/psx131)
- Kron, R. G. 1980, *ApJS*, 43, 305, doi: [10.1086/190669](https://doi.org/10.1086/190669)
- Kulkarni, G., Keating, L. C., Haehnelt, M. G., et al. 2019, *MNRAS*, 485, L24, doi: [10.1093/mnrasl/slz025](https://doi.org/10.1093/mnrasl/slz025)
- Laigle, C., McCracken, H. J., Ilbert, O., et al. 2016, *ApJS*, 224, 24, doi: [10.3847/0067-0049/224/2/24](https://doi.org/10.3847/0067-0049/224/2/24)
- Larson, R. L., Finkelstein, S. L., Pirzkal, N., et al. 2018, *ApJ*, 858, 94, doi: [10.3847/1538-4357/aab893](https://doi.org/10.3847/1538-4357/aab893)
- Leclercq, F., Bacon, R., Wisotzki, L., et al. 2017, *A&A*, 608, A8, doi: [10.1051/0004-6361/201731480](https://doi.org/10.1051/0004-6361/201731480)
- Malhotra, S., & Rhoads, J. E. 2002, *ApJL*, 565, L71, doi: [10.1086/338980](https://doi.org/10.1086/338980)
- . 2004, *ApJL*, 617, L5, doi: [10.1086/427182](https://doi.org/10.1086/427182)
- . 2006, *ApJL*, 647, L95, doi: [10.1086/506983](https://doi.org/10.1086/506983)
- Malhotra, S., Rhoads, J. E., Pirzkal, N., et al. 2005, *ApJ*, 626, 666, doi: [10.1086/430047](https://doi.org/10.1086/430047)
- Mason, C. A., Treu, T., Dijkstra, M., et al. 2018, *ApJ*, 856, 2, doi: [10.3847/1538-4357/aab0a7](https://doi.org/10.3847/1538-4357/aab0a7)
- Matthee, J., Sobral, D., Santos, S., et al. 2015, *MNRAS*, 451, 400, doi: [10.1093/mnras/stv947](https://doi.org/10.1093/mnras/stv947)
- McLinden, E. M., Finkelstein, S. L., Rhoads, J. E., et al. 2011, *ApJ*, 730, 136, doi: [10.1088/0004-637X/730/2/136](https://doi.org/10.1088/0004-637X/730/2/136)
- McQuinn, M., Hernquist, L., Zaldarriaga, M., & Dutta, S. 2007, *MNRAS*, 381, 75, doi: [10.1111/j.1365-2966.2007.12085.x](https://doi.org/10.1111/j.1365-2966.2007.12085.x)
- Naidu, R. P., Tacchella, S., Mason, C. A., et al. 2020, *ApJ*, 892, 109, doi: [10.3847/1538-4357/ab7cc9](https://doi.org/10.3847/1538-4357/ab7cc9)
- Ota, K., Iye, M., Kashikawa, N., et al. 2017, *ApJ*, 844, 85, doi: [10.3847/1538-4357/aa7a0a](https://doi.org/10.3847/1538-4357/aa7a0a)
- Ouchi, M., Shimasaku, K., Furusawa, H., et al. 2003, *ApJ*, 582, 60, doi: [10.1086/344476](https://doi.org/10.1086/344476)
- Ouchi, M., Shimasaku, K., Akiyama, M., et al. 2008, *ApJS*, 176, 301, doi: [10.1086/527673](https://doi.org/10.1086/527673)
- Ouchi, M., Shimasaku, K., Furusawa, H., et al. 2010, *ApJ*, 723, 869, doi: [10.1088/0004-637X/723/1/869](https://doi.org/10.1088/0004-637X/723/1/869)
- Ouchi, M., Harikane, Y., Shibuya, T., et al. 2018, *PASJ*, 70, S13, doi: [10.1093/pasj/psx074](https://doi.org/10.1093/pasj/psx074)
- Planck Collaboration, Aghanim, N., Akrami, Y., et al. 2018, *arXiv e-prints*, arXiv:1807.06209. <https://arxiv.org/abs/1807.06209>
- Rhoads, J. E., Malhotra, S., Dey, A., et al. 2000, *ApJL*, 545, L85, doi: [10.1086/317874](https://doi.org/10.1086/317874)
- Rhoads, J. E., Malhotra, S., Pirzkal, N., et al. 2009, *ApJ*, 697, 942, doi: [10.1088/0004-637X/697/1/942](https://doi.org/10.1088/0004-637X/697/1/942)
- Rhoads, J. E., Malhotra, S., Stern, D., et al. 2013, *ApJ*, 773, 32, doi: [10.1088/0004-637X/773/1/32](https://doi.org/10.1088/0004-637X/773/1/32)
- Robertson, B. E., Ellis, R. S., Furlanetto, S. R., & Dunlop, J. S. 2015, *ApJL*, 802, L19, doi: [10.1088/2041-8205/802/2/L19](https://doi.org/10.1088/2041-8205/802/2/L19)
- Santos, S., Sobral, D., & Matthee, J. 2016, *MNRAS*, 463, 1678, doi: [10.1093/mnras/stw2076](https://doi.org/10.1093/mnras/stw2076)
- Schechter, P. 1976, *ApJ*, 203, 297, doi: [10.1086/154079](https://doi.org/10.1086/154079)
- Shibuya, T., Kashikawa, N., Ota, K., et al. 2012, *ApJ*, 752, 114, doi: [10.1088/0004-637X/752/2/114](https://doi.org/10.1088/0004-637X/752/2/114)
- Shibuya, T., Ouchi, M., Harikane, Y., & Nakajima, K. 2019, *ApJ*, 871, 164, doi: [10.3847/1538-4357/aaf64b](https://doi.org/10.3847/1538-4357/aaf64b)
- Sobral, D., Smail, I., Best, P. N., et al. 2013, *MNRAS*, 428, 1128, doi: [10.1093/mnras/sts096](https://doi.org/10.1093/mnras/sts096)
- Taylor, A. J., Barger, A. J., Cowie, L. L., Hu, E. M., & Songaila, A. 2020, *ApJ*, 895, 132, doi: [10.3847/1538-4357/ab8ada](https://doi.org/10.3847/1538-4357/ab8ada)
- Tilvi, V., Papovich, C., Finkelstein, S. L., et al. 2014, *ApJ*, 794, 5, doi: [10.1088/0004-637X/794/1/5](https://doi.org/10.1088/0004-637X/794/1/5)
- Tilvi, V., Pirzkal, N., Malhotra, S., et al. 2016, *ApJL*, 827, L14, doi: [10.3847/2041-8205/827/1/L14](https://doi.org/10.3847/2041-8205/827/1/L14)
- Tilvi, V., Malhotra, S., Rhoads, J. E., et al. 2020, *ApJL*, 891, L10, doi: [10.3847/2041-8213/ab75ec](https://doi.org/10.3847/2041-8213/ab75ec)
- Valdes, F., Gruendl, R., & DES Project. 2014, in *Astronomical Society of the Pacific Conference Series*, Vol. 485, *Astronomical Data Analysis Software and Systems XXIII*, ed. N. Manset & P. Forshay, 379
- Wisotzki, L., Bacon, R., Blaizot, J., et al. 2016, *A&A*, 587, A98, doi: [10.1051/0004-6361/201527384](https://doi.org/10.1051/0004-6361/201527384)
- Wold, I. G. B., Finkelstein, S. L., Barger, A. J., Cowie, L. L., & Rosenwasser, B. 2017, *ApJ*, 848, 108, doi: [10.3847/1538-4357/aa8d6b](https://doi.org/10.3847/1538-4357/aa8d6b)
- Wold, I. G. B., Kawinwanichakij, L., Stevans, M. L., et al. 2019, *ApJS*, 240, 5, doi: [10.3847/1538-4365/aace85](https://doi.org/10.3847/1538-4365/aace85)
- Yang, H., Infante, L., Rhoads, J. E., et al. 2019, *ApJ*, 876, 123, doi: [10.3847/1538-4357/ab16ce](https://doi.org/10.3847/1538-4357/ab16ce)
- Zheng, Z.-Y., Wang, J., Rhoads, J., et al. 2017, *ApJL*, 842, L22, doi: [10.3847/2041-8213/aa794f](https://doi.org/10.3847/2041-8213/aa794f)
- Zheng, Z.-Y., Rhoads, J. E., Wang, J.-X., et al. 2019, *PASP*, 131, 074502, doi: [10.1088/1538-3873/ab1c32](https://doi.org/10.1088/1538-3873/ab1c32)